5-25-2017 12:00 AM

Quantification of Cerebral Blood Flow and Oxidative Metabolism in Infants with Post-Hemorrhagic Ventricular Dilatation

Peter McLachlan, *The University of Western Ontario*

Supervisor: Dr. Keith St Lawrence, *The University of Western Ontario*
Joint Supervisor: Dr. Sandrine de Ribaupierre, *The University of Western Ontario*
A thesis submitted in partial fulfillment of the requirements for the Master of Science degree in Medical Biophysics
© Peter McLachlan 2017

Recommended Citation

Abstract

Post-hemorrhagic ventricular dilatation (PHVD) is highly predictive of mortality and morbidity among very low birth weight preterm infants. Impaired cerebral blood flow (CBF) due to elevated intracranial pressure (ICP) is believed to be a contributing factor. In this study, a hyperspectral near-infrared spectroscopy (NIRS) method of measuring CBF and the cerebral metabolic rate of oxygen ($CMRO_2$) was used to investigate perfusion and metabolism changes in patients receiving a ventricular tap (VT) based on clinical signs of elevated ICP. To improve measurement accuracy, the spectral analysis was modified to account for compression of the cortical mantle caused by PHVD and the possible presence of blood breakdown products. From 9 patients (27 VTs), a significant increase in CBF was measured (15.6%) following VT (14.6 ± 4.2 to 16.9 ± 6.6 ml/100g/min), but no corresponding change in $CMRO_2$ ($1.02 \pm .41$ ml O_2/100g/min) was observed. Post-VT CBF was in good agreement with a control group of 13 patients with patent ductus arteriosus and no major cerebral pathology (16.5 ± 7.7 ml/100g/min), while StO_2 was significantly lower in these patients (58.9 ± 12.1 versus 70.5 ± 9.1% for controls). This study demonstrates that PHVD impedes CBF; however, no change in $CMRO_2$ was observed.

Keywords

Intraventricular hemorrhage, cerebral blood flow, post-hemorrhagic ventricular dilatation, near-infrared spectroscopy, cerebral metabolic rate of oxygen

Acknowledgments

Table of Contents

List of Tables (where applicable)

List of Figures (where applicable)

List of Appendices (where applicable)

List of Abbreviations

A	Attenuation or Absorption
BBB	Blood Brain Barrier
BBP	Blood Breakdown Product
CCD	Charge Coupled Device
CMT	Cerebral Mantle Thickness
$CMRO_2$	Cerebral Metabolic Rate of Oxygen
CSF	Cerebrospinal Fluid
CW	Continuous Wave
DP	Differential Pathlength
EVD	External Ventricular Drain
FD	Frequency Domain
g	Anisotropy Factor
HbO_2	Oxygenated Hemoglobin
HHb	Deoxygenated Hemoglobin
HR	Heart Rate
ICG	Indocyanine Green
ICP	Intracerebral Pressure
IRF	Instrument Response Function
IVH	Intraventricular Hemorrhage
MABP	Mean Arterial Blood Pressure
MTF	Mean Time of Flight
NA	Numerical Aperture
NIRS	Near-Infrared Spectroscopy
OD	Optical Density
PDA	Patent Ductus Arteriosus
PHVD	Post-Hemorrhagic Ventricular Dilatation
R	Impulse Residue Function
$R_d\ (t,\ \mathbf{r}_{sd})$	Diffuse Reflectance
RTE	Radiative Transport Equation
SaO_2	Arterial Oxygen Saturation
SDD	Source Detector Distance
StO_2	Tissue Oxygen Saturation
TPSF	Temporal Point Spread Function
TPSPC	Time-Correlated Single Photon Counting
WF	Water Fraction

Chapter 1

1   Introduction

1.1   Clinical Relevance

1.1.1 Intraventricular Hemorrhage

Intraventricular hemorrhage (IVH), which is a hemorrhage or bleeding from the germinal matrix into the ventricles, or the adjacent brain, is a common condition among very low birth weight preterm neonates and can lead to life-long neurological impairment such as cerebral palsy, neurological deficits or seizures. IVH is the most common form of neonatal intracranial hemorrhage and occurs mainly in preterm infants of less than 32 weeks of gestation.[1,2] The incidence of IVH ranges across different centers but is thought to be at least 25% of very low birth weight (<1500 g) premature infants with at least 12,000 cases per year in the USA.[3–5] In Canada, Radic et al. reported that severe IVH was associated with an increased risk of mortality and neurological disability among very preterm patients ($\leq$ 30 weeks gestational age).[6] Similarly, Synnes et al. reported a 29.4% overall incidence of IVH, among neonates born at less than 33 weeks gestational age, across Canadian neonatal intensive care units.[7] In other countries the incidence rate of IVH has been reported to be even higher (42% in Korea and 64% in Iran) and was negatively correlating with gestational age and birth weight.[8,9] Despite advances in neonatal care, IVH remains a problem as its incidence is correlated with the degree of prematurity and the survival rate for the smallest premature infants continues to increase.

The pathogenesis of IVH is thought to be multi-factorial including contributions from an impaired autoregulation and the presence of a fragile germinal matrix in the premature brain. Autoregulation is the ability to maintain stable blood flow due to fluctuations in blood pressure. The germinal matrix is a highly vascularized region that produces neurons and glial cells in the developing brain, primarily between 8 and 28 weeks of gestation. The periventricular germinal matrix region decreases in thickness after 24 weeks of gestation, disappearing by approximately 35 weeks.[10] IVH begins in the periventricular germinal matrix as this region has a fragile vascular bed that is highly

susceptible to hemorrhage.[11,12] The fragility of the germinal matrix vascular bed is thought to be due to weaknesses in the blood-brain barrier (BBB).[13] Inflammation may also contribute to the pathogenesis of IVH. Preterm IVH has been associated with elevated levels of umbilical cord blood interleukins (IL-1β, IL-6, and IL-8),[14–17] inflammatory signals have been shown to cross the BBB in preclinical studies,[18] and inflammation-related protein growth factors have been proposed as biomarkers of IVH.[19,20]

Gene variants relating to inflammation, infection, coagulation, and vascular pathways have been proposed as potentially relating to IVH susceptibility. These include polymorphisms for genes that encode IL-1β, IL-6, and IL-4, tumor necrosis factor (TNF), coagulation factor V Leiden mutation, coagulation factor II polymorphism and prothrombin polymorphism.[21,22] Recently, Ment et al. have suggested gene-environment interactions as possible contributors to the development of IVH.[23]

Patients typically present with IVH within the first three days after birth. Most cases are asymptomatic and will resolve without intervention. However, in roughly a quarter of cases, IVH will progress either slowly or rapidly. When symptoms progress slowly, they present as a gradual deterioration of neurological status that may include a reduced level of consciousness, movement, tone, respiration and eye movement. When IVH progresses rapidly, patients can experience a catastrophic progression of symptoms including, bulging fontanelles, a change in the level of consciousness, decerebrate posture, and rapid decreases in blood pressure and hematocrit.

In preterm infants, routine bedside cranial ultrasound (US) can be used to diagnose and monitor IVH progression. The severity of IVH is highly predictive of the severity of symptoms, co-morbidities and mortality.[1] IVH can be divided into four grades based on the Papile classification[24] depending on the extent of bleeding and ventricle dilatation. Grade I, the mildest form, is defined by bleeding within the periventricular (subependymal) germinal matrix with no blood in the ventricles. Grade II is characterized by bleeding confined to the ventricular space (based on sagittal US). Grade III is reached when the bleeding leads to a distention of the ventricles; usually with bleeding into >50%

of the ventricular volume. Grade IV is defined by the additional presence of periventricular infarction, bleeding into the brain parenchyma, in addition to distension of the ventricles due to bleeding. Grades III and IV are considered the most severe forms and have the highest association with life-long neurological impairments and risk of further complications;[25–27] however, even Grades I and II IVH are associated with poorer neurodevelopmental outcomes.[28–30]

1.1.2 Post-Hemorrhagic Ventricular Dilatation

Following a diagnosis of IVH, cranial ultrasound is used to monitor the progression of bleeding and potential occurrence of post-hemorrhagic ventricular dilatation (PHVD), which refers to the accumulation of cerebrospinal fluid (CSF) in the ventricles of the brain. Accumulation of CSF is thought to develop due to reduced reabsorption and impaired CSF communication following IVH. As CSF is continually produced by the choroid plexus of the ventricles, this leads to their progressive enlargement, elevated ICP and compression of the surrounding brain tissue. Figure 1.1 illustrates progressive ventricular dilatation via US images.
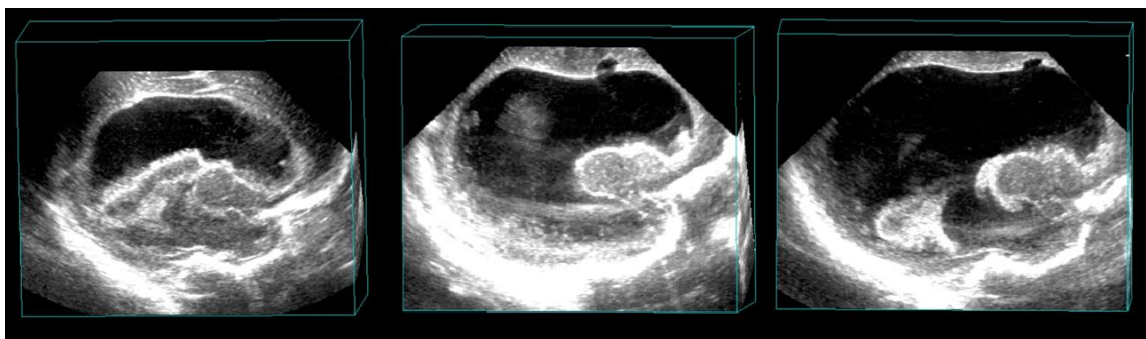
Figure 1.1: Progressive ventricular dilatation as measured by cranial US for patient in their third (left), fourth (middle), and fifth (right) weeks of life.

While mild ventriculomegaly typically resolves without intervention, up to 80% of infants with Grade IV IVH and half of those with Grade III IVH will develop PHVD, which significantly increases the risk of permanent neurodevelopmental disability (Figure 1.2).[31–33] According to the National Institute of Neurological Disorders and Stroke,

PHVD is one of the most common sources of developmental disability in children.[26,27,34,35]
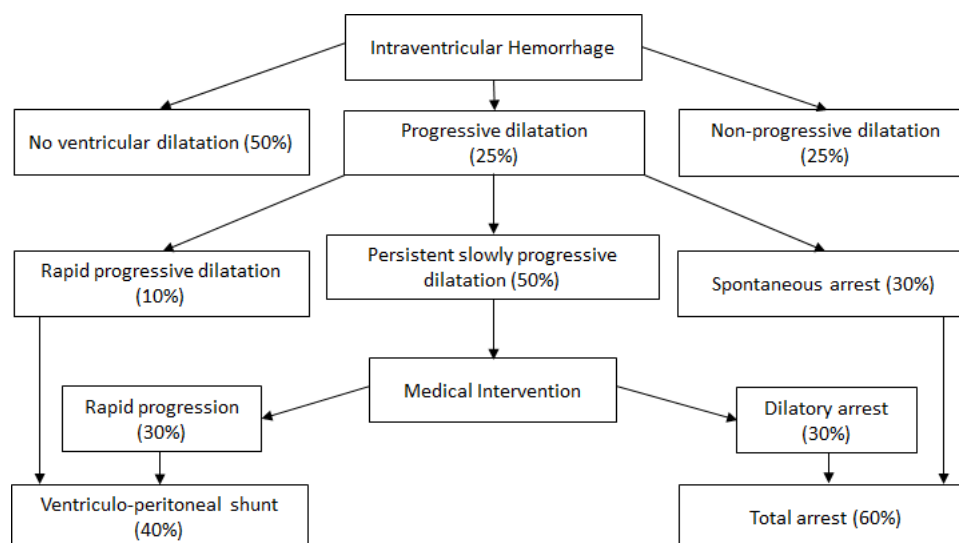
Figure 1.2: The progression and resolution of IVH and PHVD with approximate proportions of populations.

A number of potential causes have been proposed to explain PHVD. First is the blocking of cerebral aqueducts or interventricular foramina by blood clots.[36] Alternately, fibrosis of the ependymal lining caused by inflammation following IVH may contribute to PHVD as normal cilial function of the ependymal cells is required for CSF circulation.[37,38] High concentrations of pro-inflammatory cytokines have been found in the CSF of patients with PHVD. A recent study reported a causal relationship between inflammation and impaired ependymal ciliogenesis with the development of hydrocephalus. A further consideration is that elevated protein concentrations in the CSF may promote increased CSF production, to achieve osmotic balance.[39]

PHVD is currently diagnosed based on clinical assessment and US evaluation. Clinical signs of PHVD include rapidly increasing head circumference, a tense anterior fontanelle, separation of cranial sutures, and symptoms of elevated intracranial pressure (ICP; apnea, vomiting, bradycardia, abnormal posture).[40] Ultrasound can confirm suspected hydrocephalus by measuring the ventricle dimensions. The ventricular index (VI) is a composite measure of the size of the lateral and third ventricles at the level of the

foramen of Monro.[41] An abnormal score that suggests PHVD is based on an anterior horn width greater than 4 mm, a third ventricle width greater than 3 mm, and a thalamo-occipital dimension greater than 26 mm. PHVD can be defined by a VI exceeding 4 mm above the 97th percentile for gestational age.

The definitive treatment of persistent PHVD is the placement of a ventriculo-peritoneal shunt to divert CSF from the brain to the peritoneal cavity.[3] However, a shunt can become blocked by protein deposits and consequently its placement is often delayed by several weeks to allow blood clots to resolve and CSF protein levels to decrease. During this delay, intermediate interventions, such as repeated lumbar punctures, if CSF communication is preserved or ventricular decompression are often undertaken to alleviate elevated ICP. Ventricular decompression is the surgical removal of CSF by needle aspiration and is also known as a ventricular tap when performed at a single time point or as a ventricular drain when the needle and drainage apparatus is left in for a longer time period.

Frequent surveillance of the ventricular size and HC is recommended as dilatation may arrest spontaneously. Ventricular decompression carries a risk of infection and consequently the number and frequency of taps must be weighed carefully against the risk.[42,43] Given current uncertainties regarding the optimal time to perform a tapping procedure, there is a need for new methods of assessing the cerebral effects of PHVD. There is growing evidence of cerebral hemodynamic and metabolic disarrangement prior to the manifestation of clinical signs of elevated ICP. Olischar et al. reported abnormal background electrical patterns as determined by amplitude-integrated electroencephalography (aEEG) before signs of clinical deterioration, or ventricular dilatation became apparent in PHVD patients. Further, reversals in these changes were seen after CSF drainage.[44] Using transcutaneous Doppler ultrasound, Hill and Volpe measured increased cerebral blood flow velocities in infants receiving treatment for hydrocephalus.[45] Likewise, Norooz et al. found increased regional cerebral oxygen saturation as measured by near-infrared spectroscopy (NIRS) and improved aEEG patterns in patients with PHVD after ventricular decompression.[46] The NIRS results were also confirmed by a subsequent study by Soul et al.[47] These studies suggest that a means

of assessing cerebral oxygen delivery and/or energy metabolism could help guide treatment decisions in PHVD patients. NIRS is an obvious choice given measurements can be collected at the bedside, the technology is extremely safe, and it has the capabilities to measure both cerebral blood flow (CBF) and the cerebral metabolic rate of oxygen ($CMRO_2$).[48–51]

1.2 Near Infrared Spectroscopy

Near-infrared spectroscopy (NIRS) refers to a set of non-invasive, light-based methods that illuminate tissue with non-ionizing light to measure the concentrations of chromophores, which are light absorbing molecules. NIRS takes advantage of low light absorption by tissue in the near-infrared range (650 - 1000 nm), which enables light to penetrate beyond superficial layers and probe tissues up to a couple of centimeters deep. Importantly, there are only a few endogenous chromophores that exhibit distinct absorption features within the NIR window. These characteristic spectral features enable the concentrations of the chromophores to be differentiated. In particular, by determining the concentrations of oxy and deoxy-hemoglobin, tissue oxygen saturation can be calculated.

1.2.1 History of NIRS

The development of quantitative optical methods began in the 1940 when Glenn Millikan invented the muscle oximeter.[52] Expanding on the ex-vivo work by Chance and Weber,[53] Jobsis performed the first in-vivo cerebral NIRS measurements in 1977. Jobsis demonstrated that the translucency of the scalp and skull allowed changes in cortical oxygenation caused by hyperventilation to be measured in adults.[54] In 1985, NIRS monitoring of cerebral oxygenation was performed in neonates by Brazy et al.[55] and in adults by Ferrari et al.[56] Delpy and colleagues reported quantitative measurements of various parameters in newborns including changes in oxy- and deoxyhemoglobin concentrations, total hemoglobin concentration, blood volume and blood flow in 1986.[57] In 1988, Cope et al. demonstrated that absolute changes in chromophore concentrations could be measured if the optical pathlength through tissue was assumed.[58] Soon after,

Delpy et al. made measurements of the mean optical pathlength, opening the door for absolute chromophore quantification.[59]

The three primary endogenous chromophores in brain tissue within the NIR range are water, oxy-hemoglobin, and deoxyhemoglobin and their absorption spectra are shown in Figure 1.3. Their absorption properties are responsible for forming the local minimum in light absorption within the NIR range known as the 'optical window.' The upper limit is formed by the rapid increase in absorption by water above 920 nm. The lower limit of around 650 nm is due to the strong absorption by hemoglobin below this point. Within these limits, there is minimum light absorption, which enables light and hence NIRS methods to probe deeper tissues. By measuring absorption at multiple wavelengths, the absorption contribution from these and other chromophores (cytochrome oxidase and lipids) can be determined. Although water is a relatively weak absorber in the NIR range, it is found in such high concentrations in tissue (about 85% in the neonatal brain) that its effects on absorption in tissue are measureable. In addition, its distinct absorption features at 740 and 840 nm make it possible to separate it from oxy and deoxy-hemoglobin.
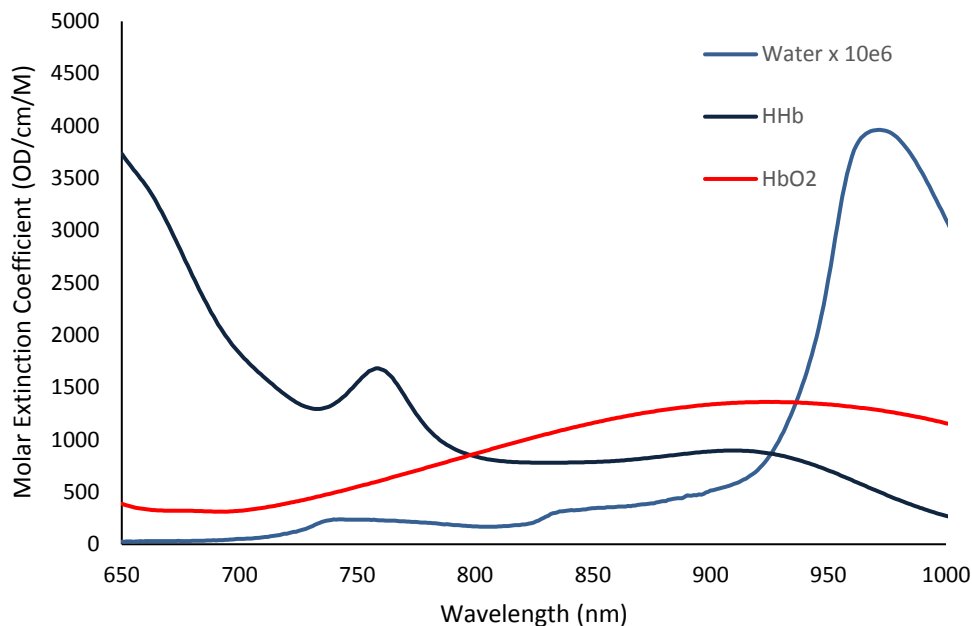
Figure 1.3: Molar extinction coefficients for the three most important endogenous NIR chromophores: deoxyhemoglobin (HHb) and oxyhemoglobin (HbO$_2$) Water has been multiplied by 10^6 to be visible.

The most important endogenous chromophore is hemoglobin because of its strong absorption, which changes with oxidation state. This fundamental property enables NIRS to discriminate between deoxy-hemoglobin (HHb) and oxy-hemoglobin (HbO$_2$) if light absorption is measured at a minimum of two wavelengths. The most commonly used NIRS oxygenation measure is regional tissue oxygen saturation (StO$_2$), which is determined from [HbO$_2$] and [Hb] by the following:

$$StO_2 \ = \frac{[HbO_2]}{[Hb]+[HbO_2]}$$

(1.1)

1.2.2 Physical Principles of NIRS

Light is attenuated when travelling through tissue by two primary interactions: absorption and scattering. The total light absorption depends on the wavelength-dependent properties of the chromophores present in tissue. Since absorption is proportional to chromophore concentration, it is the property most relevant to biomedical NIRS

applications. However, the primary interaction of light with tissue is by scattering, which varies with wavelength and depends on the size of particles within the tissue. Characterization of the attenuation of light within tissue requires understanding both of these effects. The basics of NIRS absorption and scattering are discussed in this section.

As light propagates through a medium, light energy is transferred to particles in the medium, which can excite the particles to a higher energy state. When this results in a transfer of energy without the reemission of another photon, absorption has occurred. The mechanism of light absorption depends on wavelength. Low-energy NIR photons interact with matter non-destructively and energy is typically transferred by exciting molecular bonds, primarily by altering the dipole moment of a bond. Therefore chromophores must have one or more bonds that are able to change in dipole moment due to the vibrational energy excitation of a photon interaction.[60]

Qualitatively, absorption is the reduction in light intensity while travelling through a non-scattering medium. Bouguer first described in 1729 the loss of intensity as light travels through a medium. Lambert extended this idea to state that this absorbance was directly proportional to the thickness of the medium (i.e. the path length of the light). The fraction of light absorbed dI/I is then proportional to the thickness of an infinitesimal layer, dl, by a constant of proportionality referred to as the absorption coefficient, μ_a.

$$\frac{dI}{I} = \mu_a dl \tag{1.2}$$

By integrating, we can derive the Lambert-Bouguer law.

$$I = I_0 e^{-\mu_a l} \tag{1.3}$$

In 1852, Beer extended this law by relating μ_a to the concentration of a light absorber, c, in the medium, (Figure 1.4) which is known as the Beer-Lambert law:

$$A = -log\left(\frac{I}{I_0}\right) = \mu_a l = \varepsilon \cdot c \cdot l \tag{1.4}$$

where, A is the absorbance and ε is the molar extinction coefficient of the chromophore.
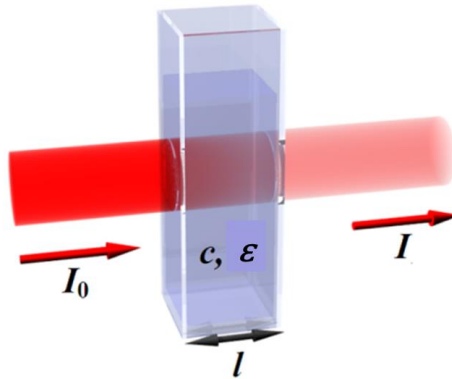
Figure 1.4: The absorption of light through a non-scattering medium is a function of the chromophore concentration, the molar extinction coefficient and the path length.

In the presence of multiple light absorbers the Beer-Lambert law can be extended linearly to include the contributions of each chromophore, as follow:

$$A = \varepsilon_1 \cdot c_1 \cdot l + \varepsilon_2 \cdot c_2 \cdot l + \ldots = \sum_i \varepsilon_i \cdot c_i \cdot l . \tag{1.5}$$

Light scattering refers to the dispersion and redirection of light from its straight trajectory. It is the most common interaction and the major source of attenuation within tissue. As light travels through tissue it encounters tissue boundaries, cell membranes, and large particles such as organelles, and will be reflected, refracted or redirected at each of these interfaces. Light scattering can be characterized in terms of scattering by particles that are small relative to the wavelength of light (Rayleigh scatter), larger structures (Mie scattering) such as nuclei and mitochondria of sizes on the order of the wavelength of light, about 1000 nm, and at interfaces between media with differing indices of refraction (Fresnel reflection). The most common mechanisms of scattering in the NIR range are Mie scattering and Fresnel reflection. Rayleigh scattering becomes more significant as the wavelength decreases and has only a minor contribution in the NIR range. Fresnel reflection refers to scattering that occurs at cell membranes which are much larger than the wavelength of NIR light and can therefore be considered boundaries between different media.[61] Due to the vast number of such interfaces encountered by light in tissue, scattering is best described statistically. Mathematically, the attenuation of light due to scattering can be described by exponential decay:

$$I = I_0 e^{-\mu_s l} \tag{1.6}$$

where, μ_s is the scattering coefficient which represents the probability that a photon will experience a scattering event per unit length. The intensity, I, is a measure of non-scattered light and is a function of direction, area, and position. Within tissue, scattering events far outnumber absorption events as different modes of scattering events may take place in succession and light becomes rapidly diffused. Scattering makes it difficult to model light propagation in tissue and complicates quantitative spectroscopy. The wavelength dependency of scattering can be approximated heuristically by a power law:[62]

$$\mu_s' = A \left(\frac{\lambda}{500 \text{ (nm)}} \right)^{-\alpha} \tag{1.7}$$

where A and α are constants determined experimentally or predicted by a combination of Mie and Rayleigh scattering.[63] A thorough understanding of light scatter is essential for biomedical optical techniques, particularly in the use of Monte Carlo modelling to be discussed later.

To accurately describe the behavior of light in tissue, we need to consider the directionality of scattering. The scattering angle can be described by the Henyey-Greenstein phase function, which was originally developed to describe light scattering by small particles in interstellar dust clouds.[64] This probability density function gives the likelihood of scattering events as a function of angle, θ, given a factor, g, describing scattering anisotropy in the medium:

$$p(\theta) = \frac{1}{4\pi} \frac{1-g^2}{(1+g^2-2g\cos\theta)^{3/2}} \tag{1.8}$$

The anisotropy factor, g, of a tissue is the statistical mean cosine of the scattering angle and can vary between 0 and 1. Most tissues have a high g value, around 0.9, meaning high anisotropy, or primarily forwarded directed scattering events. However, within a diffusive medium light will undergo multiple scattering events, and rapidly lose directionality. At this point light transport is best described by diffusion and the light is said to be in the 'diffusion regime.' In this case it is useful to assume isotropic, non-directional, scattering occurring with a probability of the scattering coefficient reduced by a factor of $1 - g$. This probability, μ_s', known as the transport scattering coefficient, or

the reduced scattering coefficient, is a lumped parameter that describes the diffusion of photons through a r walk process of step-size $1/\mu_s'$.

$$\mu_s' = \mu_s(1 - g) \tag{1.9}$$

To perform quantitative in-vivo spectroscopy, several consequences of scattering must be considered. First, light in tissue will rapidly diverge and so at any detector position the detected light will be of a small fraction of the intensity of transmitted light. Second, due to multiple scattering events the mean path length travelled by photons will be much greater than the geometrical distance between the light source and detector. The mean path length will depend on the optical properties of the medium as well as the distance between emitter and detector. Additionally, scattering is wavelength dependent and so attenuation will be increased at shorter wavelengths where scattering is greater. To overcome these obstacles, the Beer-Lambert law can be replaced by the modified Beer-Lambert law for scattering media:

$$A(\lambda) = DP(\lambda)\sum_i \varepsilon_i C_i + G(\lambda). \tag{1.10}$$

where A is attenuation, DP is the differential path length (the mean path length taken by light in a scattering medium), ε_i is the molar absorption coefficient of the ith absorber, and C_i is the concentration of the ith absorber, and G is a term representing the proportion of light not detected due to scattering. A number of techniques have been developed to account for the effects of scattering and are discussed in Section 1.3.

1.3   Modelling Light Propagation in Tissue

1.3.1 The Diffusion Approximation

The behaviour of NIR light, like any form of electromagnetic radiation, is governed by Maxwell's equations. However, in a complex, heterogeneous, highly scattering medium, analytical solutions to Maxwell's equations are impractical to obtain. Closed form solutions are further complicated by non-static scattering particles in tissues that are in a constant state of Brownian motion. To overcome these problems, it more useful to describe light as discrete photons that are elastically scattered and absorbed and governed

by the radiative transfer equation (RTE), also known as the Boltzmann transport equation:

$$\left[\frac{1}{v}\frac{\partial}{\partial t} + \hat{s}\cdot\nabla + \mu_a + \mu_s\right]L(\boldsymbol{r},t,\hat{s}) = \mu_s\int_{4\pi} L(\boldsymbol{r},t,\hat{s})P(\hat{s},\hat{s}')d\Omega' + S(\boldsymbol{r},t,\hat{s}) \qquad (1.11)$$

where $L(\boldsymbol{r},t,\hat{s})$ is the radiance in the medium (units of W/m^{2}sr) as a function of position $\boldsymbol{r}$ in the direction defined by unit vector $\hat{s}$. The RTE is a balance equation describing the conservation of energy within a medium. Other parameters include the velocity of light in the medium, v, the scattering phase function, $P(\hat{s},\hat{s}')$, the source term, $S(\boldsymbol{r},\hat{s},t)$ representing power injected into a unit volume, and the solid angle around $\hat{s}$. Unfortunately because of the complexity of the RTE, it has no general analytical solution and must be solved by numerical methods.

The RTE can be greatly simplified for diffusive media, such as tissue, in which scattering is much stronger than absorption (ie. $\mu_s' \gg \mu_a$) and the radiance is nearly isotropic. Under these assumptions, the radiance is equal to the sum of an isotropic fluence, ϕ, in units of energy or photons per unit volume, plus a small directional flux $\vec{J}$:

$$\frac{1}{v}\frac{\partial\phi(r,t)}{\partial t} + \nabla\cdot\vec{J}(r,t) + \mu_a\phi(r,t) = S(r,t) \qquad (1.12)$$

Since $\vec{J}(\boldsymbol{r},t) = -D\nabla\,\phi(\boldsymbol{r},t)$, the diffusion approximation (DA) can be rewritten in terms of ϕ only:

$$\left(\frac{1}{v}\frac{\partial}{\partial t} - D\nabla^2 + \mu_a\right)\phi(\boldsymbol{r},t) = S(\boldsymbol{r},t), \qquad (1.13)$$

where D is known as the diffusion constant:

$$D \equiv \frac{1}{3[(1-g)\mu_s+\mu_a]} \equiv \frac{1}{3[\mu_s'+\mu_a]}. \qquad (1.14)$$

Analytical solutions for particular boundary conditions can be obtained for the DA. For these solutions, the source is assumed to be an isotropic point and the scattering isotropic within the medium, simplifying the phase function to a constant factor. Assuming the source can be represented by an infinitesimal short pulse of light, the time-dependent solution to the DA for an infinite medium is given by:

$$\phi(\mathbf{r},t) = v(4\pi Dt)^{-3/2}\,exp(\mu_a vt)\,exp\left(\frac{-r^2}{4\pi Dt}\right) \qquad (1.15)$$

1.3.2 Monte Carlo Modelling

The DA provides accurate results for larger source-detector distances (SDDs), in which the detected photons can be considered to be in the diffusion regime (i.e. to propagate isotropically) for relatively simple geometries, such as a semi-infinite medium. An alternative approach that does not rely on either of these conditions is Monte Carlo modeling. This is a statistical approach that can model light propagation outside of the DA, such as at small SDDs and for arbitrary propagation geometries.[65,66]

Using probability functions to describe the likelihood of interactions between light and the medium, the behavior of vast numbers of independent photons can be simulated computationally. The simulated medium can be heterogeneous in terms of optical properties and of arbitrary geometry. Figure 1.5 outlines a simplified block diagram of the parallel Monte Carlo simulation of photon migration. In a heterogeneous simulation volume the optical properties of the medium are a function of position and boundary effects between media must also be considered.
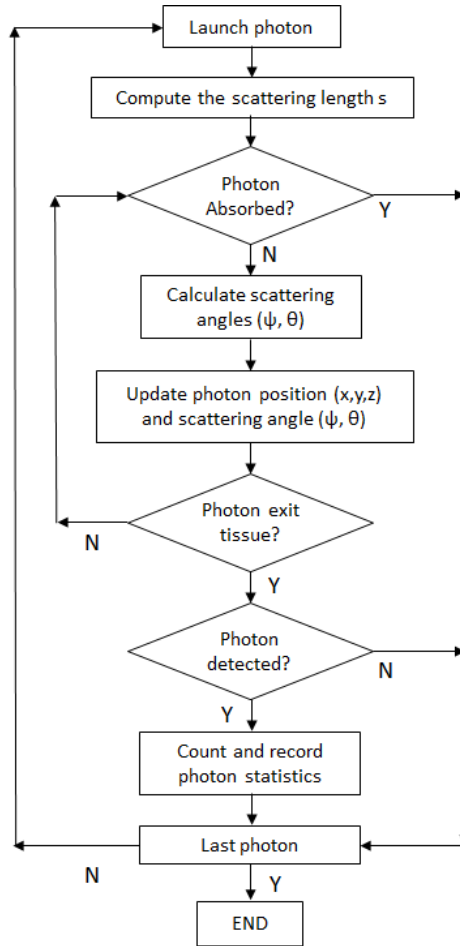
Figure 1.5: Simplified flowchart for Monte Carlo simulation of light propagation in tissue.

Monte Carlo modelling launches virtual photons into a volume at a user-defined position and direction. The distance until the first scattering event, or step size, is calculated based on the probability of a scattering event, defined by μ_s. The probability of a photon having a particular step size is given by the following non-uniform probability density function:

$$p(s) = \mu_s e^{-\mu_s s} \tag{1.16}$$

To sample this probability density function, a pseudorandom number, ξ, on the interval of 0 to 1 is generated and will satisfy the following relationship:

$$\int_0^x p(x)dx = \xi \tag{1.17}$$

Substituting equation 1.16 into equation 1.17, integrating and replacing ξ with (1- ξ) due to symmetry about 0.5, yields the following non-uniform random variable:

$$s = -\frac{\ln(\xi)}{\mu_s} \tag{1.18}$$

Next, the random scattering direction can be calculated. The scattering direction is defined by sampling the azimuthal angle $\psi \in [0,2\pi]$ and the elevation angle $\theta \in [0, \pi]$. The azimuthal angle is sampled uniformly over $[0,2\pi]$, and the elevation angle is determined by sampling the Henyey-Greenstein function giving following random variable θ:

$$\theta = \begin{cases} \cos^{-1}\left\{\frac{1}{2g}\left(1 + g^2 - \left[\frac{1-g^2}{1-g+2g\xi}\right]^2\right)\right\} & for\ g \neq 0 \\ \cos^{-1}(2\xi - 1) & for\ g = 0 \end{cases} \tag{1.19}$$

Photons are assumed to be continuously attenuated by absorption during this process. At each successive scattering event the photon weight, or energy of the photon packet, can be calculated as a fraction of the packet's initial weight. The reduction in weight, ΔW, is calculated as

$$\Delta W = \frac{\mu_a}{\mu_a + \mu_s} W. \tag{1.20}$$

By numerically sampling these three functions, Monte Carlo simulations allow the accurate modeling of light propagation within an arbitrary volume. The geometry and optical properties of the simulation volume can be specified by the user, and based on models of the head. When this process is repeated for millions of photons, the fluence within the simulation volume can be described spatially and temporally, and analyzed identically to actual NIRS data. Simulations of large numbers of independent photons is highly parallelizable and therefore the entire process can be accelerated by simultaneously computing the behavior of many photons using modern graphics processing units (GPUs).[67]

1.4   Methods of In-vivo Spectroscopy

There are a number of NIRS techniques that can be explained in terms of the type of light source and detection methods used. This section provides an overview of some of the

most commonly methods. All approaches presented attempt to provide quantitative measurements of chromophore concentrations by separating the effects of light absorption and scattering.
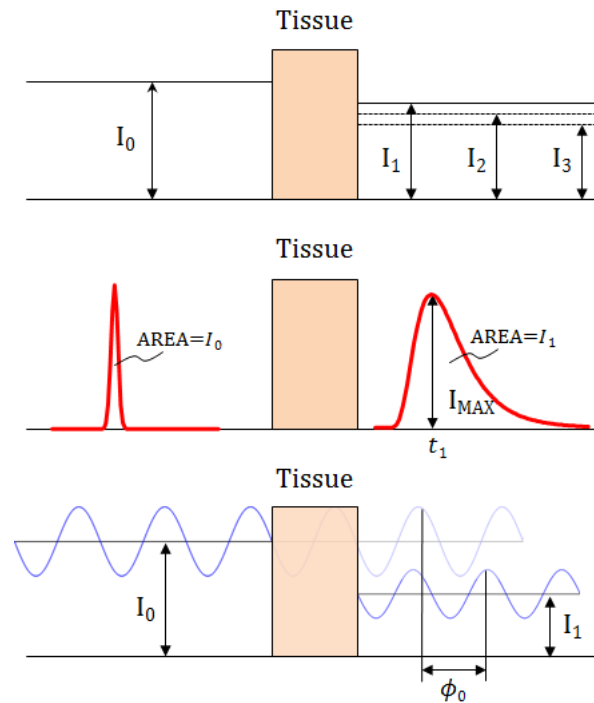
Figure 1.6: A pictorial comparison of common NIRS methods: spatially resolved spectroscopy (top), time-resolved NIRS (middle) and frequency-domain NIRS (bottom). I_0 and I_1 denote input and detected intensities, while ϕ_0 denotes phase difference. All methods analyze the transport of light through tissue in order to extract information about the optical properties of the medium. In spatially resolved spectroscopy light intensities at various source detector distances are compared. In time-resolved spectroscopy the temporal distribution of detected photons is analyzed. Frequency-domain NIRS relies on measuring phase and amplitude changes in the reflected light.

1.4.1 Spatially Resolved Spectroscopy

Spatially resolved spectroscopy (SRS) is a technique first demonstrated by Matcher et al in 1995[68] and it is the basis of many commercial systems (Figure 1.6). This technique requires relatively simple equipment including continuous discrete light sources and

inexpensive photodiodes for detection. Quantification is achieved by measuring light attenuation at multiple source-detector pairs.

If we consider a semi-infinite, refractive index-matched geometry with a collimated light source incident at the surface ($z = 0$) at $r = 0$ and a detector at $r = r_{sd}$, then the diffuse reflectance (light intensity in units of energy or photons) as a function of r_{sd}, $R_d(r_{sd})$ is given by[69]

$$R_d(r_{sd}) = \frac{z_0}{2\pi} \frac{exp\left[-\mu_{eff}(z_0^2+r_{sd}^2)^{1/2}\right]}{z_0^2+r_{sd}^2}\left[\mu_{eff} + \frac{1}{(z_0^2+r_{sd}^2)^{1/2}}\right],$$ (1.21)

where z_0 ($\approx 1/\mu_s$) is the depth at which the source can be considered to be isotropic and has entered the diffusion regime. The effective attenuation coefficient, μ_{eff}, is defined as

$$\mu_{eff} \equiv \sqrt{3\mu_a(\mu_a + \mu_s')} \approx \sqrt{3\mu_a \mu_s'},$$ (1.22)

since $\mu_s' \gg \mu_a$. When r_{sd} is large, ($r_{sd} \gg z_0$), which is true for commercial NIRS devices where r_{sd} is typically around 3 to 4 cm, equation 1.21 can be simplified to

$$R_d(r_{sd}) = z_0 \frac{exp(-\mu_{eff}r_{sd})}{2\pi\, r_{sd}^2}\left[\mu_{eff} + \frac{1}{r_{sd}}\right].$$ (1.23)

Multiplying this expression by r_{sd}^2 and taking the natural logarithm, yields

$$\ln[r_{sd}^2\, R_d(r_{sd})] = -\mu_{eff}\, r_{sd} + \ln\left(\mu_{eff} + \frac{1}{r_{sd}}\right) + constant.$$ (1.24)

When $r_{sd} \gg \mu_{eff}$ the second term becomes a constant and a linear relationship is obtained between $\ln[r_{sd}^2\, R_d(r_{sd})]$ and r_{sd} with a slope of $-\mu_{eff}$ as follows:

$$\ln[r_{sd}^2\, R_d(r_{sd})] = -\mu_{eff}\, r_{sd} + intercept.$$ (1.25)

Thus by plotting $\ln[r_{sd}^2\, R_d(r_{sd})]$ versus r_{sd}, for at least two source detector separations (r_{sd}) a direct estimate of μ_{eff} can be obtained from the slope. As μ_{eff} is a function of μ_a and μ_s', to measure each independently, additional information is required. Patterson et al. proposed measuring the total diffuse reflectance, $R_d(r_{sd})$, over the entire surface in order to give the transport albedo and is which is equal to $\mu_s'/(\mu_s' + \mu_a)$.[70] Other means of

estimating μ_s' are available; for example, μ_s' can be estimated from $R_d(r_{sd})$ at small r_{sd}. Liu et al. have proposed a method for using calibrated values of $R_d(r_{sd})$ in order to solve for the intercept in equation 1.25 which can be manipulated to yield μ_s'.[71] More typically, μ_s' of the brain is set to an experimentally measured value.[62]

1.4.2 Time-Resolved NIRS

Time-resolved near-infrared spectroscopy (TR-NIRS) was first introduced in 1988 by Chance et al.[72] and Delpy et al.[59] The technique relies on transmitting ultra-short pulses (frequently in the picosecond range) of light into the medium and measuring the temporal point spread function (TPSF) of transmitted light intensity with a detector with picosecond resolution (Figure 1.7). Because they require the use of ultrafast detectors and emitters, TR systems are more expensive and technically more complicated than CW systems. However, TR NIRS is quantitative as the mean optical path length can be directly measured from the mean time of flight (MTF) of photons. Furthermore, μ_a and μ_s' can be determined by modelling the TPSF by the diffusion approximately. For example, the time-dependent solution to the diffusion approximation for a semi-infinite geometry is given by the following:

$$R_d(r_{sd}, t) = (4\pi D)^{-3/2} z_0 t^{-5/2} \, exp(-\mu_a v t) \, exp\left(\frac{-r_{sd}^2 + z_0^2}{4Dt}\right) \qquad (1.26)$$
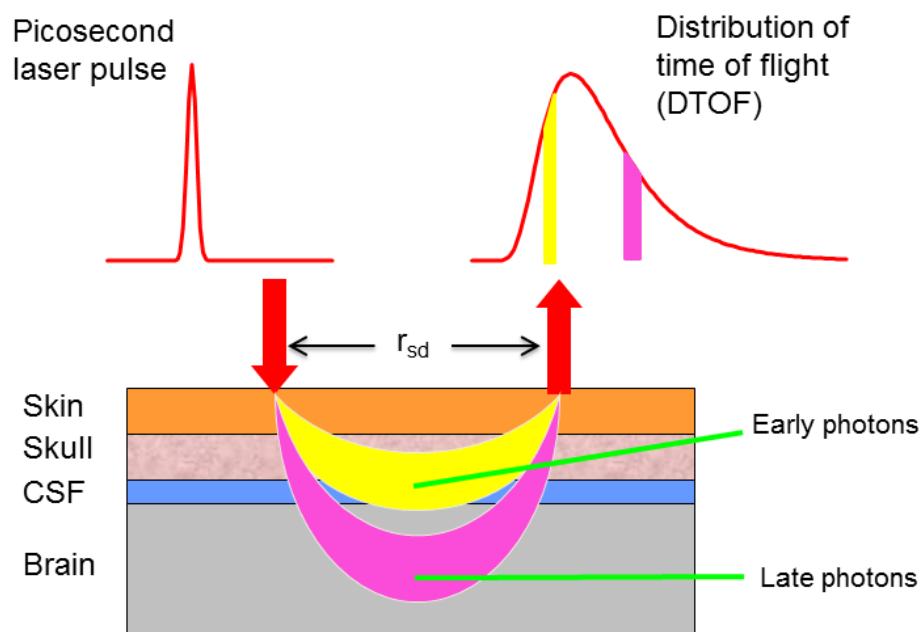
Figure 1.7: In time-resolved NIRS picosecond laser light pulses are transmitted into the medium and the TPSF of photons reaching the detector is recorded. Early arriving photons have a shorter optical path length and are more sensitive to the extra-cerebral tissue layers. Late arriving photons travel further and so have more sensitivity to deep tissues like the brain.

1.4.3 Frequency Domain NIRS

Frequency domain (FD) NIRS was first introduced by Chance et al. in 1990[73] and further developed by Duncan et al.[74] and Fantini et al.[75] FD-NIRS uses intensity-modulated light sources in the radio frequencies range, typically around 100 MHz. The light sources used are commonly inexpensive laser diodes or light emitting diodes (LEDs). The detectors measure light intensity (DC component) as well as the phase of the modulation light (AC component). When intensity-modulated light is transmitted through tissue, the phase of the intensity at the detector is related to the mean optical path length (Figure 1.6). In this sense FD NIRS is the frequency analogue of TR NIRS.[76] As a result, changes in the amplitude and phase of detected light provide a method of measuring of absorption coefficient [75,77] from which absolute chromophore concentrations can be calculated. Due

to the need to modulate the light source and the requirement for fast detectors capable of capturing phase changes, FD NIRS systems are more complex than CW systems, but are less expensive than TR instrumentation. The main drawback of FD systems is phase noise.[77]

1.4.4 Second Derivative Spectroscopy

Second derivative spectroscopy, which was developed by Matcher and colleagues in the 1990's, measures light attenuation over the entire NIR range.[78] This approach requires a broadband white light source to illuminate tissue and a spectrometer to detect reflected light intensity as a function of wavelength. This method takes advantage of the fact that the differential path length, DP, and the scattering term, G, in the modified Beer-Lambert law, equation 1.10, are only weakly dependent on wavelength. If scattering is assumed to have an approximately linear dependence on wavelength, then its contribution to the second derivative of the measured attenuation spectrum is negligible. Consequently derivatives of DP and G vanish from the second derivative of equation 1.10, leaving the following relationship between the second derivative of the attenuation spectrum (A) and chromophore concentrations:

$$\frac{\partial^2 A(\lambda)}{\partial \lambda^2} = DP(\lambda) \sum_i \frac{\partial^2 \varepsilon_i(\lambda)}{\partial \lambda^2} C_i \tag{1.27}$$

With this approach, the mean differential path length (DP), can be determined by assuming a known tissue concentration of water. In brain the water concentration is approximately 85%[48] which is known to be quite stable.[79] With DP measured, the HHb concentration can be determined by its unique absorption feature around 760 nm (Figure 1.8). Another advantage of derivative spectroscopy is it eliminates the effects of any DC effects such as caused by imperfect coupling between optical fibres and the tissue.
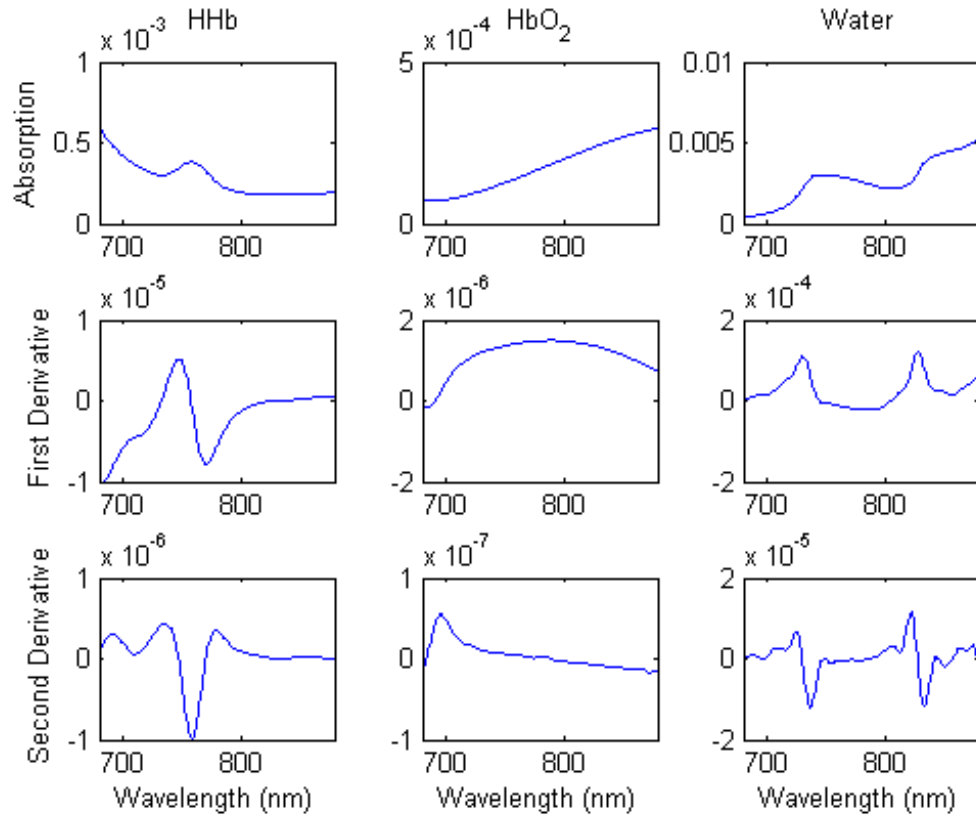
Figure 1.8: Endogenous NIR chromophore absorption spectra (top row) and their corresponding 1st and 2nd derivative spectra for HbO_2, HHb and water.

A disadvantage of this approach is the HbO_2 concentration cannot be determined reliably, as it has no discernable second derivative features. However, this approach can be modified to overcome this issue by applying the diffusion approximation to both the first and second derivative spectra, which will be described in in section 2.4.

1.4.5 NIRS Monitoring of Cerebral Hemodynamics and Metabolism

The brain typically exhibits a high rate of oxygen metabolism[80] and as such it is dependent on a consistent and regulated supply of oxygen. Therefore monitoring the supply of oxygen to the brain can be essential to assessing the impact of disease, particularly with cerebrovascular disorders.

As discussed earlier, the most commonly used NIRS index is StO_2, primarily because it only requires relative HHb and HbO_2 measurements (equation 1.1). Consequently, multiple inexpensive commercial CW NIRS systems are available that provide continuous StO_2 monitoring.[81] It is important to note, however, that StO_2 is a composite indicator that depends on CBF, arterial oxygenation and the cerebral metabolic rate of oxygen ($CMRO_2$). Because it cannot be directly related to either blood flow or oxygen utilization, some investigators have questioned if it represents the best marker of brain health.[82] To overcome this, NIRS methods have been developed to directly measure CBF. The first approach used was a version of the Kety-Schmidt method[83] wherein small changes in arterial oxygen saturation are induced as a blood flow tracer.[84]

Alternatively indocyanine green (ICG), which is an FDA-approved optical dye, can be used as an intravascular contrast agent.[85,86] The advantage of this approach is the considerable improvement in contrast to noise ratio due to the strong and distinctive absorption properties of ICG (Figure 1.9). Upon bolus injection, ICG rapidly binds to plasma proteins,[87] which restricts it to the blood pool, until removed from the circulation by the liver with a biological half-life on the order of a few minutes. The details of this dynamic contrast-enhanced (DCE) NIRS method will be provided in more detail in section 2.4.
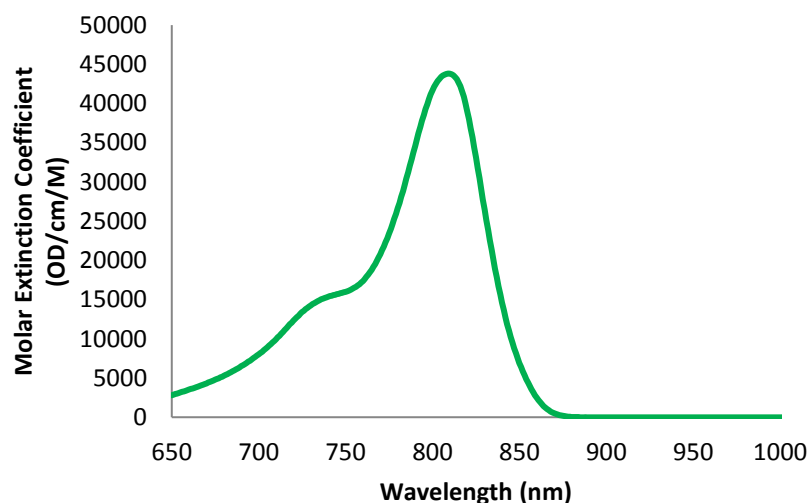
Figure 1.9: The specific absorption spectrum of ICG.

A limitation of these bolus tracking approaches are that they only provide a single time-point measurements of CBF. An alternative approach for measuring blood flow continuously that does not require a flow tracer is diffuse correlation spectroscopy (DCS),[88–90] which is sensitive to blood flow due to the temporal signal fluctuations, known as speckle, caused by the movement of red blood cells. DCS measures blood flow changes by quantifying temporal fluctuations of NIR light reflected from a tissue. Light that passes through the scalp and skull enters the brain, where it is scattered by moving red blood cells within blood vessels. A portion of this light is reflected back to the tissue surface where it reaches the detector. Dynamic scattering from moving red blood cells causes the detected light intensity to fluctuate in time. The temporal intensity fluctuations can be used to generate an autocorrelation function, which in turn can be characterized by a version of the DA that includes a term to account for blood flow. The shape of the autocorrelation function has been shown to be correlated with tissue blood flow; however, the derived blood flow index is only a relative measure of CBF. One approach to get around this issue has been to combine continuous DCS data with a single measurement of CBF determined using ICG as a blood flow tracer.[91]

The $CMRO_2$ can be determined by combining NIRS measurements of StO_2 and CBF. This approach is based the Fick principle, which defines $CMRO_2$ from a mass balance equation. Namely, the rate that oxygen is consumed in brain tissue is equal to the difference between the amount delivered, which is proportional to CBF multiplied by the arterial saturation, and amount leaving, which is proportional to CBF multiplied by the cerebral venous saturation. Further details are given in Chapter 2.

Clinical NIRS studies have reported relatively low CBF (~ 15 ml/100g/min) and $CMRO_2$ (~ 1 ml O_2/100g/min) in the preterm brain compared to adults, reflecting the developmental state of the brain at this early age.[50,51,92,93]

1.5   Research Objectives

PHVD patients present a challenge to NIRS as ventricular dilatation and increased ICP leads to considerable reductions in the thickness of surrounding brain tissue (i.e., cerebral mantle). NIRS analysis techniques typically rely on the assumption that the reflected light

predominately interrogates brain tissue. For patients with severe PHVD, the cerebral mantle can be reduced to roughly a centimeter, enabling light to penetrate ventricle space. An additional complication is the presence of blood breakdown products (BBP) in the ventricle following IVH. In the case of grade IV IVH, BBP could also be present in the surrounding tissue. Many BBP, including bilirubin, biliverdin, and methemoglobin, are strong NIR absorbers; however, NIRS analysis typically equates measured absorption to only oxy-hemoglobin, deoxy-hemoglobin and water.

To address these challenges, the first goal of this study was to modify a previously developed hyperspectral (broadband) NIRS technique to account for variations in cerebral mantle thickness and possible BBP contamination.[48] With this approach, measured spectra were analyzed using a solution to the diffusion approximation based on a slab geometry of finite-thickness to account for cortical mantle compression.[94] Cortical thickness measurements were obtained from concurrent 2D US images. The chromophore quantification fitting routine was also modified to incorporate an experimentally derived BBP absorption spectrum.

The second goal of this study was to predict how cortical mantle compression and the presence of BBP within the ventricular CSF could affect StO_2 estimates derived with SRS using the standard semi-infinite solution to the diffusion approximation. Error analysis was conducted by Monte Carlo simulations for absorption measurements at two wavelengths and two SDD to reflect SRS approaches commonly used by commercial NIRS systems.

The final objective of this work was to use broadband NIRS to investigate possible changes in CBF, StO_2, and $CMRO_2$ in PHVD patients selected to undergo a ventricle tap based on clinical assessment. Given the association of clinical signs such as apnea and bradycardia with elevated ICP, it was hypothesized that the tapping procedure would lead to an increase in CBF. The effects on $CMRO_2$ were less certain considering that lower CBF can be compensated for by an increase in the oxygen extraction fraction (OEF).[95] The acquired spectra and hemodynamic measurements were also compared to data from a control group consisting of premature neonates diagnosed with patent ductus arteriosus

(PDA). This group was from a previous study and was chosen as none of the patients had major cerebral pathologies including moderate or severe IVH.[48]

Chapter 2

2   Methods

2.1   Patient Population

As part of a prospective study, patients admitted into the neonatal intensive care unit and diagnosed with IVH on routine cranial ultrasound were enrolled following informed parental consent. IVH was graded based on the severity scale by Papile et al.[24] Between April 2011 and February 2015, 57 patients were enrolled in the study, and of those, 10 neonates developed PHVD that required interventional therapy. Ventricle taps (VTs) were used as the initial intervention based on clinical signs of increased ICP (spells of apnea and bradycardia, full and tense fontanelles), and qualitative evidence of increased ventricle size measured by ultrasound. Decisions on when to intervene were based on current clinical practice and the care team was blinded to the NIRS measurements during the study period. The study protocol was approved by the Research Ethics Board of Western University (London, Ontario).

NIRS data from a previous study involving 13 preterm neonates (<30 weeks gestational age) diagnosed with PDA was used as the control group.[48] These patients were selected to represent a normal population as none of the patients had a diagnosis of moderate or severe IVH (grade II-IV, Papile classification) or any major congenital malformation of the brain. The group mean StO_2 (70.5 $\pm$ 2.4%) was within the expected range for stable preterm infants. Data acquisition was performed with the same broadband NIRS system used to acquire the spectra from the PHVD patients.

2.2   Study Design

After the decision to perform a VT was made by the neurosurgery team, two NIRS data sets were acquired: one 5 - 10 min prior to and the other 10 - 60 min after the VT. The range was greater for the post-tap acquisitions as it was delayed in neonates that required resuscitation. NIRS data were acquired from the fronto-parietal cortex by probes placed on the scalp and held in place by a custom-built holder strapped to the infant's head.

Probes were repositioned to the same approximate head position for post VT measurements. The DCE NIRS protocol consisted of collecting a spectrum every 200 ms for a total duration of 80 s with ICG (0.1 mg/kg at a concentration of 0.5 mg/ml sterile water, BCD Pharma, Mississauga, Ontario, Canada) injected via a pre-existing venous catheter at the 10-s mark. The time-varying arterial ICG concentration was recorded simultaneously by a dye densitometer (DDG-2001 A/K, Nihon Kohden, Tokyo, Japan) attached to a foot.

Mean arterial blood pressure (MABP), arterial oxygen saturation (SaO$_2$), heart rate (HR), transcutaneous partial pressure of carbon dioxide (TcPCO$_2$), and head circumference (HC) were recorded before and after VT. Other recorded clinical measures included the mode of ventilation and the total hemoglobin concentration, which was used to calibrate the arterial ICG concentration curve. The cerebral mantle thickness (CMT) was measured from a coronal ultrasound image taken within 24 hours of the VT through the anterior fontanelle at the level of the foramen of Monro. The CMT was calculated as the average distance measured from the ventricular border to the skull, lateral and superior to the ventricles on the head side of the NIRS probes (Figure 2.1).
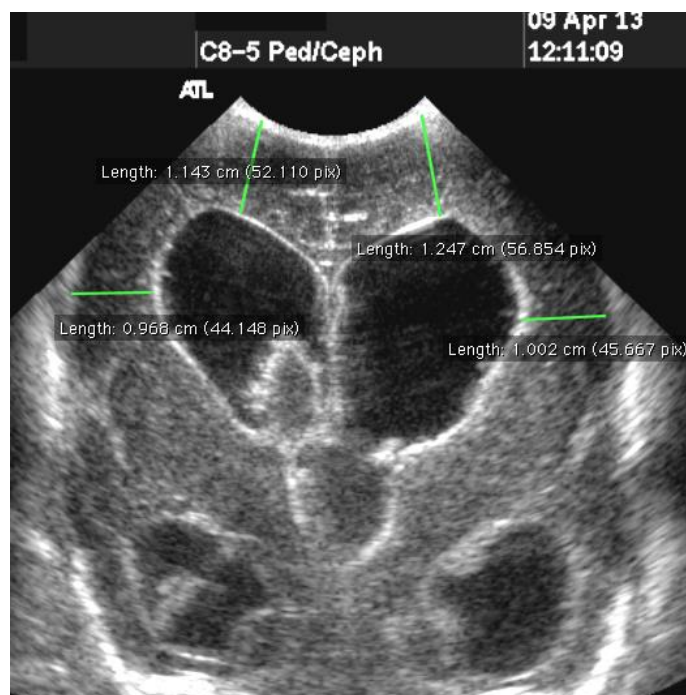
Figure 2.1: An ultrasound image used to generate a CMT estimate of 11 mm (left and right sides). The CMT Is calculated as the mean of distances measured from the ventricular border to the skull, lateral and superior to the ventricle.

2.2.1 CSF Analysis

Spectral analysis was conducted on 2-ml samples of CSF collected during the VT. The absorption spectrum for each sample was determined with a spectrophotometer (Beckman DU-640, Beckman Coulter, USA) with respect to distilled water as a reference. As CSF is 99% water in healthy patients this additional absorption was attributed to BBPs. The mean absorption spectrum of all samples was incorporated into the chromophore quantification fitting procedure (see section 2.4 Data Processing).

For the purpose of error analysis simulations, the CSF samples were divided into two groups based on the principle colours observed (yellow and red). Average absorption values for each group were included in Monte Carlo simulations performed to assess the influence of ventricular CSF on SRS StO_2 measurements (see section 2.5 Error Analysis).

The scattering properties of CSF samples were assessed by measuring the TPSF of transmitted light (760 nm) using a previously developed TR NIRS system.[91,96,97] The TR system consisted of a picosecond pulsed diode laser (LDF-P-C-810, PicoQuant, Germany) emitting at 802 nm coupled by a microscope objective lens (NA = 0.25, magnification = 10X) to a 1.5m long multimode fiber (NA = 0.22, 400 μm core; Fiberoptics Technology, Pomfret, CT). The laser output was 1.4 mW and the pulse repetition rate was 80 MHz. Two variable neutral density filters (NDC-50-4M, Thorlabs, Newton, NJ) placed between the laser and optical fiber were used to adjust the power delivered to the samples. Transmitted light was collected with a 2 m fiber optic bundle (NA = 0.55, 3.6 mm active area; Fiberoptics Technology) and delivered to a Peltier-cooled photomultiplier tube (PMC-100, Becker & Hickl, Germany). Photon detection generated an electrical pulse that was transmitted to a time-correlated single photon counting (TCSPC) module (SPC-134, Becker & Hickl, Germany). Because the TCSPC module had a dead time of 100 ns, the count rate was adjusted to a typical rate of 800 kHz (1% of the laser pulse repetition rate) to minimize dead-time and pile-up effects.[98]

The TPSFs of two CSF samples (one yellow, one red) and a reference water sample were measured in a transmittance mode with a source-detector separation of 2 cm by placing each sample in a custom 3D-printed polymer cuvette. The average of three hundred TPSFs were collected per sample and characterized by calculating the mean transit time and the full width at half maximum (FWHM). Since light scattering in pure water is relatively small,[99,100] these parameters were used to assess potential increases in scattering in the CSF samples.

2.3 Instrumentation

NIRS measurements were acquired with an in-house developed, continuous-wave broadband NIRS system (Figure 2.2).[48] The main components of the system are a 20-W halogen light bulb (Ocean Optics HL-2000-HP), with a band-pass filter to remove light outside the NIR range, and a spectrometer consisting of a holographic diffraction grating housed in a light-tight box (Sciencetech Inc., London, ON Canada) coupled to a Peltier-cooled CCD camera (Wright Instruments Ltd, UK). The CCD chip was 1024 x 124 pixels in dimension and was operated as an array detector by binning the 124-pixel axis of the

CCD. The spectrometer has a spectral range of 680 to 980 nm and a resolution of 0.38 nm per pixel. The light was delivered to the head by a 2-m long fiber optic bundle (3.5 mm diameter, 0.55 numerical aperture). The detection fiber bundle had the same properties and collected reflected light at an interoptode distance of 3 cm.

Figure 2.2: In-house developed, continuous-wave broadband NIRS system mounted on a cart for bedside use, consisting of a diffraction grating spectrometer (Sciencetech Inc., ON, Canada), coupled to a charge coupled device (CCD) camera (Wright Instruments, UK).

2.4 Data Processing

2.4.1 Quantifying Chromophore Concentrations

Photon flux through the head can be modelled using solutions to the diffusion approximation for specific geometries. The most commonly used solution is for a semi-

infinite medium, which is typically considered acceptable for infants as signal contamination from extra-cerebral tissues is small at source-detector separations of around 3 cm and greater.[101] The adaptation of this approach to spectral analysis has been described previously.[102,103] With this approach, the wavelength dependency of μ'_s is modelled by:[62]

$$\mu'_s(\lambda) = A\left(\frac{\lambda}{800}\right)^{-\alpha} \tag{2.1}$$

where A is the value of μ'_s at 800 nm. The absorption coefficient is defined in terms of the three main endogenous chromophores in brain tissue (HHb, HbO$_2$, water):

$$\mu_a(\lambda) = [HbO_2] \cdot \varepsilon_{HbO_2}(\lambda) + [HHb] \cdot \varepsilon_{Hb}(\lambda) + WF \cdot \varepsilon_{H_2O}(\lambda) \tag{2.2}$$

where $\varepsilon_i(\lambda)$ represents the molar extinction coefficient of the ith chromophore and WF is the water fraction in tissue. For DCE NIRS, equation 2.2 was expanded to include the molar extinction coefficient of ICG.

Two modifications were made to the model to accommodate the analysis of spectra from PHVD patients. First, the solution to the diffusion approximation for a semi-infinite medium was replaced by the solution for a slab geometry, of known finite thickness, representing the thinned cortical mantle (see Figure 2.1). This solution is composed of an infinite series of terms representing photon flux from virtual sources of increasing distances, both positive and negative, from the true source location.[94] Only the first five terms were included in the solution as this was found to be sufficient to provide convergence. The CMT was measured from US imaging as outlined in the section 2.2. The second modification was to add an additional chromophore to the definition of μ_a to account for possible light absorption from BBPs:

$$\mu_a(\lambda) = [HbO_2] \cdot \varepsilon_{HbO_2}(\lambda) + [HHb] \cdot \varepsilon_{Hb}(\lambda) + WF \cdot \varepsilon_{H_2O}(\lambda) + k \cdot \mu_{a,BBP}(\lambda) \tag{2.3}$$

where $\mu_{a,BBP}$ is the mean absorption spectrum across all CSF samples (in units of inverse length), and λ is the wavelength. The average absorption spectrum of all samples was used as differentiating between the red and yellow group averages did not have a

significant impact on the chromophore fitting. The scaling factor, k, is included as the exact concentration of breakdown products in the samples were not measured.

Spectral analysis began by applying a wavelet de-noising algorithm that consisted of transforming Poisson noise to Gaussian noise, removing the latter by wavelet de-noising, and applying an inverse transformation to obtain noise-reduced spectra.[104] Smoothing was performed using a 5-point moving average filter before generating a derivative spectrum to minimize noise contributions.

Chromophore concentrations were determined by fitting the solution to the diffusion approximation to the first and second derivatives of measured reflectance data, $R(\lambda)$ using five fitting parameters: [HbO$_2$], [HHb], WF, A and α. First, WF was determined by fitting the second derivative spectrum of $R(\lambda)$ to the water feature between 815 and 840 nm, a range devoid of any hemoglobin features (see Figure 1.8). Using this WF estimate, [HHb] was determined by fitting the second derivative spectrum of $R(\lambda)$ to the distinct 760 nm HHb feature over the range from 680 to 775 nm. Finally, [HbO$_2$], k, and the scattering parameters A and α were determined by fitting the first derivative spectrum of $R(\lambda)$ from 680 to 840 nm with WF and [HHb] fixed to the values obtained previously. Fitting was performed using a constrained optimization routine based on the MATLAB script *fminsearchbnd* with upper and lower boundaries set to span published values.[102] [HbO$_2$] and [HHb] were determined from the mean spectrum acquired before ICG was injected and used to calculate StO$_2$ according to equation 1.1.

Cerebral blood flow was determined from the DCE NIRS approach mentioned in section 1.4.5. With this approach, the passage of the dye through the brain microvasculature is modelled as a linear, time-invariant system. With this approach, the time-varying ICG concentration in brain, C$_t$(t), is related to CBF and the corresponding arterial concentration curve, C$_a$(t) by:

$$C_t(t) = C_a(t) * CBF \cdot R(t) \qquad (2.4)$$

where $*$ indicates the convolution operator, and $R(t)$ is referred to as the impulse residue function. It represents the amount of ICG in brain following an ideal bolus injection of unit concentration.[105] The flow-scaled impulse residue function, $CBF \cdot R(t)$, is extracted

from $C_t(t)$ and $C_a(t)$ by deconvolution.[91] The initial height of this function is equal to CBF since by definition $R(t)$ has an initial value of one, ie. $R(t = 0)$ is zero.

The CMRO$_2$ was calculated based on the Fick principle:

$$CMRO_2 = \frac{CBF \cdot K}{f_v} \cdot [tHb] \cdot (SaO_2 - StO_2) \qquad (2.5)$$

where K represents the oxygen carrying capacity of hemoglobin (1.39 ml of O$_2$ per g of Hb) and f_v is the venous fraction of cerebral blood volume and is assumed equal to 0.75.[91]

2.5 Error Analysis

To test for potential errors caused by a decreased CMT and the presence of BBP chromophores within the ventricular CSF, simulated StO$_2$ data were generated by Monte Carlo modelling. Data were generated for a two-layer planar model designed to represent the two dominant tissues (brain and ventricles) in the PHVD head. Simulations were conducted for two wavelengths (730 and 810 nm) and two source-detector pairs (3 and 4 cm), as these parameters are commonly used by commercial CW-NIRS systems.[81] Simulated light propagation was performed using the CUDAMCML[106,107] software package. Photon reflectance data were generated for a range of the thicknesses for the top layer (10 to 30 mm) to reflect the range of the CMT observed clinically. The simulated data were analyzed by SRS, which again is commonly used by most commercial NIRS systems. Source-detector distances of 3 and 4 cm were chosen as they have been shown to be relatively insensitive to signal contamination from extra-cerebral tissues. At each CMT and each wavelength, one billion photons were launched into the simulation volume and the reflected light intensity recorded at the specified detector positions.
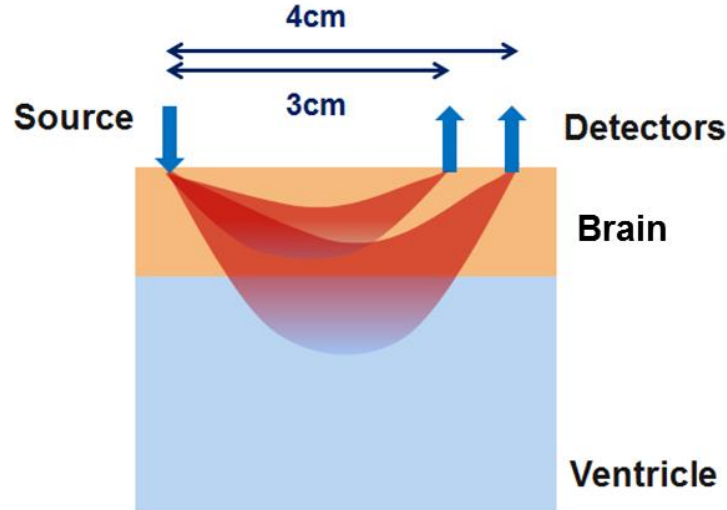
Figure 2.4: The simulation volume comprised of two layers (brain, ventricular CSF). Diagram also shows the two source-detector pairs.

The absorption coefficient of the brain was set using equation 2.2 with a total hemoglobin concentration (tHb) of 15 g/dL, [HHb] and [HbO$_2$] values corresponding to StO$_2$ = 70%, a water fraction of 85%[48] and μ_s' of 1 mm^{-1}.[108] For the ventricle layer, μ_s' = 0.01 mm^{-1} [109] and μ_a was varied over three conditions representing red, yellow and clear CSF (0.066, 0.0096, 0.0021 mm^{-1}, respectively, at 730 nm and 0.059, 0.0075, 0.0022 mm^{-1}, respectively, at 810 nm). The μ_a values for red and yellow CSF were set to the values measured by spectrophotometry and μ_a for clear CSF was set to literature values for water.[100]

StO$_2$ was calculated using the SRS approach outlined in section 1.4.1.[110] Briefly, taking the log of the reflected light intensity, $R(r)$, scaled by the square of the source-detector separation, r, results in the following:

$$\ln[R(r) \cdot r^2] = r \cdot Slope + Intercept \tag{2.6}$$

where, *Slope* is the slope of the reflectance loss between two r values and is given by:

$$Slope = \frac{\mu_a}{3(\mu_a + \mu_s')} \cong \frac{\mu_a}{3\,\mu_s'} \tag{2.7}$$

If μ_s' is assumed, typically 1 mm^{-1},[101,109] then μ_a can be computed based on equation 2.7 from the measured slope. [HHb] and [HbO$_2$] can be determined from the μ_a values measured at 730 and 810 nm according to following relationship:[81]

$$\begin{bmatrix} [HHb] \\ [HbO_2] \end{bmatrix} = A^{-1} \begin{bmatrix} \mu_a(\lambda_1) \\ \mu_a(\lambda_2) \end{bmatrix}, \quad A = \begin{bmatrix} a_{HHb,\lambda_1} & a_{HbO_2,\lambda_1} \\ a_{HHb,\lambda_2} & a_{HbO_2,\lambda_2} \end{bmatrix}. \tag{2.8}$$

where $a_{i,j}$ are the absorption coefficients of HHb and HbO$_2$ at wavelengths j. Then StO2 can be calculated from equation 2.4.

2.6 Statistical Analysis

Non-parametric tests were used to assess the statistical significance of results. Mann-Whitney U tests were performed to assess the difference before and after VT for CBF, StO$_2$, CMRO$_2$ as well as SaO$_2$, HR, MABP, and TcPCO$_2$. Wilcoxon Signed-Rank tests were used to determine significance between pre-VT PHVD data and the control group. Statistical significance of all tests was based on a P value of < 0.05. Data are presented as mean ± standard error (SE) unless stated otherwise.

Chapter 3

3 Results

3.1 CSF Samples

When collected serially, sample colour was initially dark red and transitioned to paler and paler yellow over time. The CSF samples collected during VT were found to fall into one of two categories based on colour (dark red or yellow) which are shown in Figure 3.1. This categorization was not unexpected given that common hemoglobin breakdown products may include ferritin and methemoglobin (dark brown/red) and bilirubin (straw coloured).[111,112] The mean absorption spectrum for each group is illustrated in Figure 3.2. Spectra for individual CSF samples were normalized to their value at 650 nm to account for absorption variations due to concentration differences. The mean spectrum across all samples, which was used in the fitting procedure, is also shown. Although the samples could be separated based on colour by visual inspection, the NIR spectra all displayed the same general shape, of decreasing absorption observed with increasing wavelength. Given that the absorption spectrum of both oxy-hemoglobin and methemoglobin increase from 700 to 1000 nm,[113] the measured spectra suggest that the CSF samples contained a significant concentration of bilirubin, which has been reported to exhibit a similar wavelength dependency to that seen in the samples.[61]
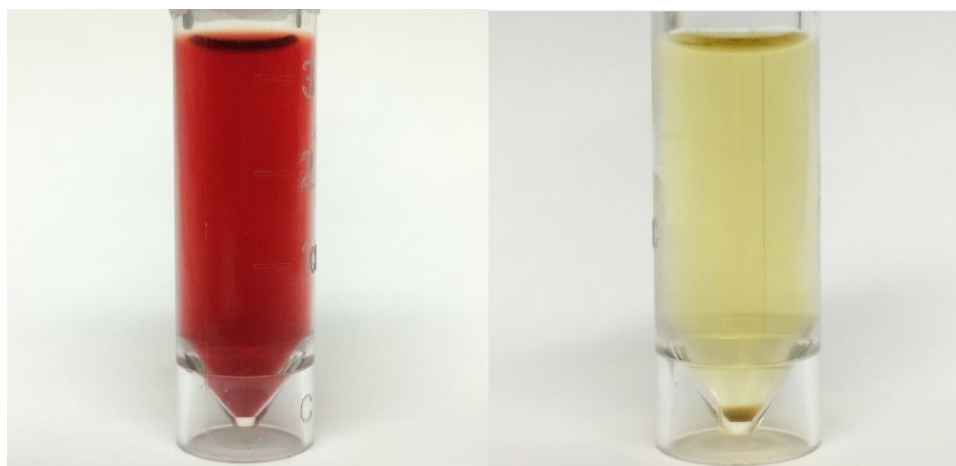
Figure 1: Representative red and yellow CSF samples
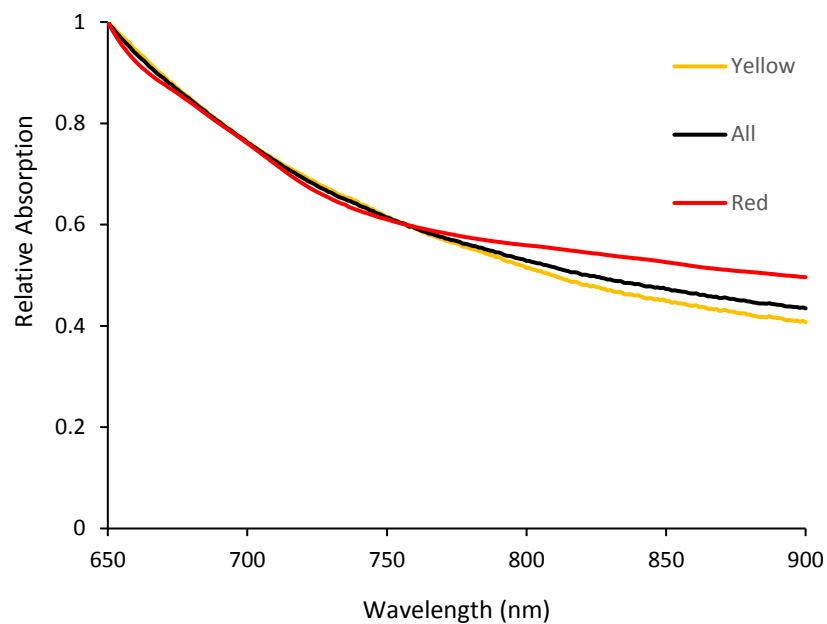
Figure 3.2: Mean absorption spectra for the red and yellow CSF sample groups (4 and 9 samples respectively) along with the mean of all samples (black).

The FWHM of the measured TPSFs for the yellow and red CSF samples (560 and 585 ps, respectively) were very similar to that of water (559 ps) shown in Figure 3.3. Likewise the mean transit times of the yellow (466 ps) and red (470 ps) of the CSF samples were only 2% and 9% greater than that of water (462 ps). The close agreement between the mean transit times and FWHM of these three samples indicates that they have negligible scattering effects in the NIR range.
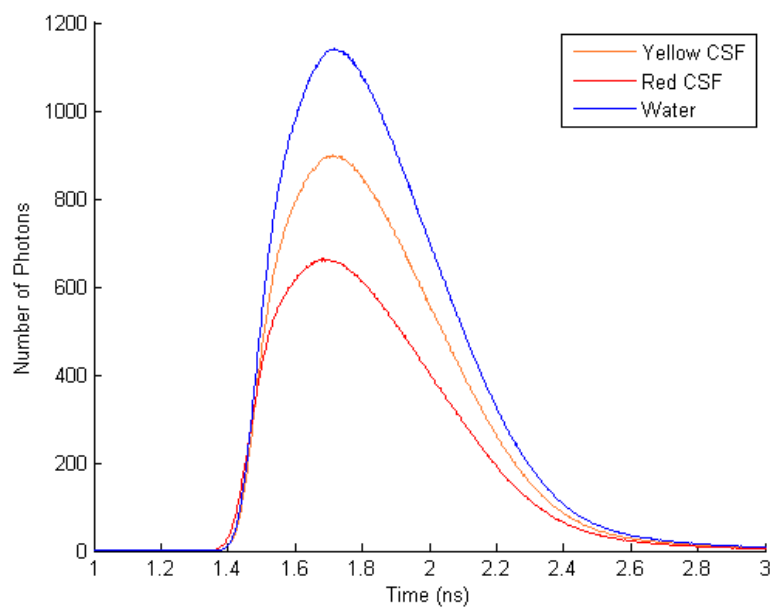
Figure 3.3: TPSFs of photons through CSF and water samples in transmittance mode.

3.2   Patients Studied

NIRS data were acquired from ten patients who required multiple VTs. In total, 27 taps were monitored. Data from three patients (7 taps) were excluded due to sizable artifacts in the arterial ICG curves caused by excessive foot motion. One additional set was removed due to the poor quality of the NIRS spectra, which was attributed to ambient light contamination. The remaining 20 taps from 9 patients were analyzed and the clinical measures of those patients are summarized in Table 3.1. Also, included in Table 3.1 are the relevant clinical data from the control group (N = 13).[48] The Apgar score is a cumulative value received by a newborn on a scale of 0 to 2 over five criteria: Appearance (skin colour), Pulse (heart rate), Grimace (reflexes), Activity (muscle tone), Respiration (breathing rate and effort). The maximum Apgar score is 10.

	PHVD patients	Controls
Gestational Age at birth (weeks ± SD, [range])	26.9 ± 1.8 [24 6/7 - 29]	27 [24 3/7-35 5/7]
Birth Weight (g ± SD, [range])	1011 ± 206 [750-1280]	1035 [630-2135]
Sex	M=6, F=3	M=8, F=5
Apgar 1 min (mean, [range])	2.9 [1-8]	4 [2-8]
Number of VT required (mean, [range])	2.4 [1-5]	0
Age at first VT (days ± SD [range])	17.7 ± 8.7 [7-35]	n.a.
EVD (N)	2	n.a.
VP Shunt (N)	7	n.a.
Neonatal death (N)	1	0
Cortical Mantle Thickness (cm)	1.23 ± 0.3 [0.96-1.74]	n.a.
IVH (N)		
Bilateral III	4	0
Grade IV(R)/III(L)	3	0
Grade IV(L)/III(R)	1	0
Bilateral IV	1	0

Table 3.1: Clinical parameters of the 9 neonates with PHVD who required interventional ventricle tap. SD = standard deviation, EVD = extraventricular drain, VP = Ventriculoperitoneal shunt.

3.3 Absorption Spectra

Figure 3.4A presents the measured pre-tap spectrum from one PHVD patient with a CMT of 11 mm and diagnosed with bilateral Grade III IVH. For comparison, the figure includes the mean absorption spectrum from the control group. Figure 3.4B presents theoretical absorption spectra generated from the diffusion approximation for a semi-infinite medium and an 11-mm thick slab. Spectra were generated with identical tissue properties (StO$_2$ = 0.7, μ'_s = 1 mm^{-1}, water fraction = 0.85, and tHb = 150 g/L) to

illustrate the effects of a finite turbid layer thickness on the predicted reflectance spectrum.
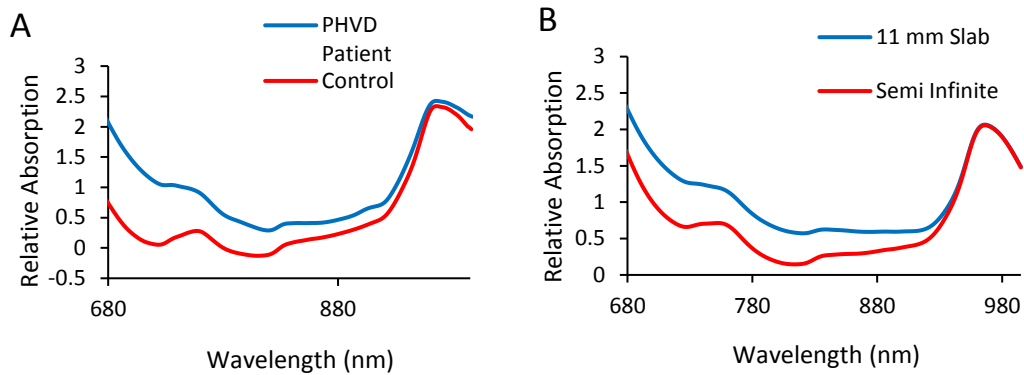
Figure 3.4: A) Measured head spectra from the control group (red) and a PHVD patient with CMT = 11 mm B) Simulated absorption spectra based on the principle chromophores (water and hemoglobin) in the brain using a semi-infinite (red) and 11-mm slab model (blue).

Average first and second derivative spectra, pre and post-VT, are shown in Figure 3.5. Each patient's spectrum was averaged over 50 repetitions acquired in the 10-s period prior to ICG injection. For reference, each graph includes the corresponding mean derivative spectrum for the control group. In general, the pre and and post-tap second derivative spectra were very similar to the control spectrum, specifically at the 760 nm Hb feature and water feature between 815 and 840 nm. In contrast, there was a noticeable downward shift in the first derivative spectra from the PHVD patients compared to control group; however, the differences between pre- and post-tap spectra were considerably smaller.
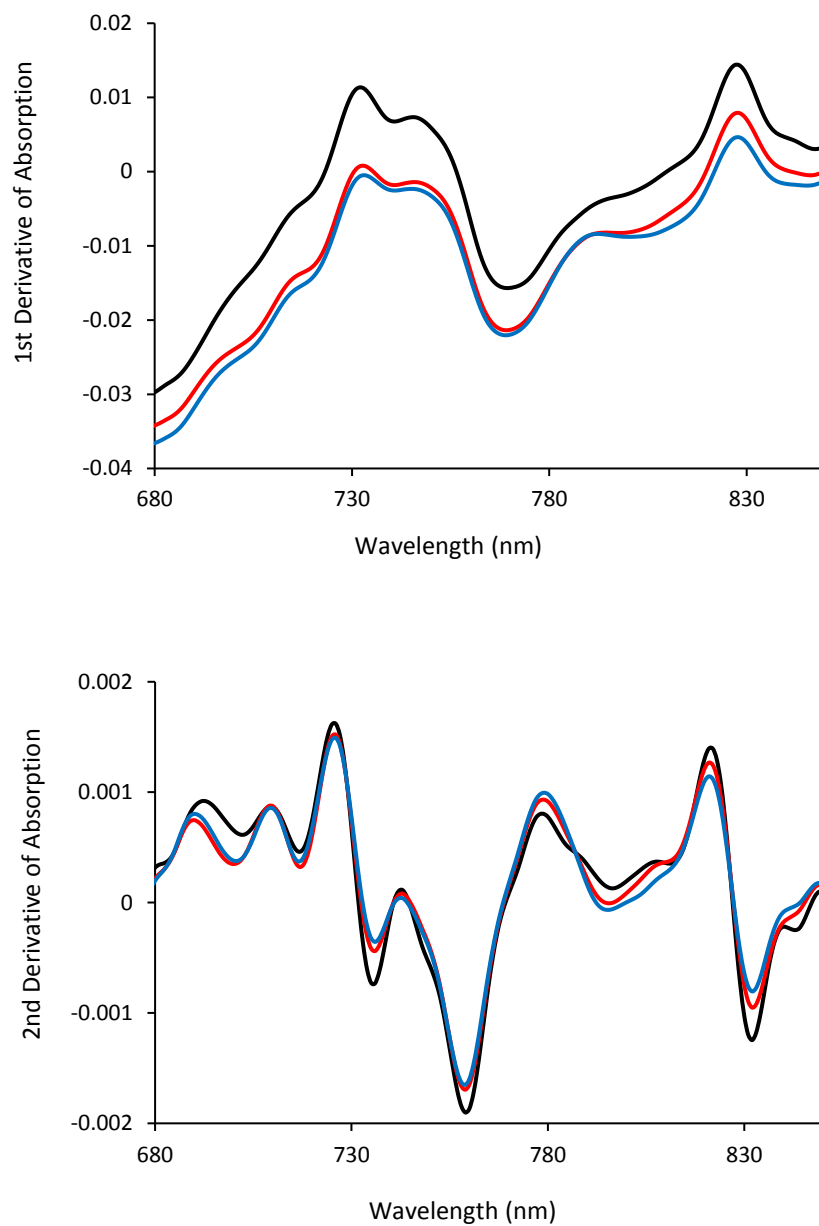
Figure 3.5: Average first and second derivative spectra prior to (blue) and after (red) tap. Each graph also includes the corresponding spectrum from the control group (black)

3.4 ICG Concentration Curves

Figure 3.6 illustrates tissue ICG concentration curves measured by DCE NIRS acquired pre and post VT from one infant. In this example, CBF increased by 14.7% from 13.4 to 15.4 mL/100g/min.
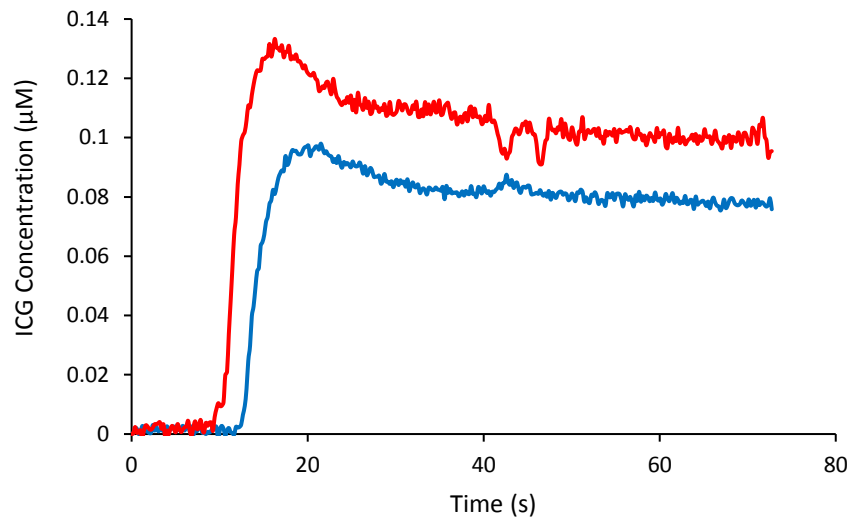
Figure 3.6: Example ICG concentration curves measured by DCE NIRS pre (blue) and post (red) VT from a patient with bilateral grade III IVH. ICG is injected at around the 10 second mark. The cerebral blood flow is related to the rate of increase of ICG concentration in the brain.

3.5 Pre and Post Ventricle Tap

Table 3.2 provides the average values of the fitting parameters from the spectral analysis, as well as CBF and $CMRO_2$ before and after VT. Values were averaged over 20 data sets. A statistically significant (p-value < 0.01) average increase in CBF of 15.6% was observed following the tapping procedure, along with a significant increase in [HbO_2] by 14.2%. Corresponding differences in [HHb], StO_2, OEF, and $CMRO_2$ were small and did not reach significance. Likewise, there were no significant changes in the two scattering parameters, although the difference in α pre and post VT was close to significant. Also included in the table are the clinical parameters measured pre and post VT. Among the

clinical data, only head circumference (HC) showed a significant change after the procedure with a reduction of about 1 cm.

Parameter	Pre	Post	Change (%)	Significance (*P value*)
CBF (ml/100g/min)	14.6 ± 1.0	16.9 ± 1.5	15.6	**0.006**
[HHb] (μM)	15.2 ± 1.0	16.4 ± 1.4	10.2	0.50
[HbO$_2$] (μM)	26.3 ± 4.6	30.0 ± 4.4	11.9	**0.035**
tHb (μM)	41.5 ± 4.8	46.4 ± 4.8	12.0	0.075
SaO$_2$ (%)	92.7 ± 0.8	91.8 ± 0.8	-1.0	0.13
StO$_2$ (%)	58.9 ± 2.7	61.0 ± 2.8	3.1	0.35
CMRO$_2$ (ml O$_2$/100g/min)	1.00 ± 0.08	1.04 ± 0.10	4.9	0.33
OEF	0.36 ± 0.03	0.34 ± 0.03	-7.1	0.078
A (mm^{-1})	0.37 ± 0.04	0.34 ± 0.03	-7.3	0.22
α	3.9 ± 0.32	4.4 ± 0.30	16	0.055
HC (cm)	28.4 ± 0.1	27.5 ± 0.1	-3.1	**< 0.001**
HR (bpm)	157 ± 0.4	159 ± 0.5	1.5	0.19
MABP	51.8 ± 0.6	48.9 ± 0.5	-5.7	0.21
TcPCO$_2$	54.4 ± 0.8	56.5 ± 0.7	3.9	0.37

Table 3.2: Group-averaged parameters before and after ventricle tap (mean $\pm$ standard error, N = 20).

3.6 Comparison between PHVD Patients and Controls

Average values of the spectral fitting parameters, CBF, OEF and CMRO$_2$ from the PHVD group (pre-VT) and controls are given in Table 3.3. Significant decreases in StO$_2$ and [HbO$_2$] along with a corresponding increase in OEF were observed when comparing PHVD patients to controls. However, no significant differences in CBF and CMRO$_2$ between the two groups were observed. Interestingly, α, which describes the wavelength dependency of scattering, was significantly higher in the PHVD group.

Parameter	Controls	PHVD	Difference (%)	Significance (*P value*)
CBF (ml/100g/min)	16.5 ± 2.1	14.6 ± 1.0	-11.8	0.32
[HHb] (μM)	12.9 ± 0.9	15.2 ± 1.0	17.9	0.051
[HbO$_2$] (μM)	32.0 ± 4.2	26.3 ± 4.6	-17.9	**0.043**
tHb (μM)	44.9 ± 4.0	41.5 ± 4.8	-7.7	0.20
StO$_2$ (%)	70.5 ± 2.4	58.9 ± 2.7	-16.4	**0.004**
CMRO$_2$ (ml O$_2$/100g/min)	0.90 ± 0.14	1.00 ± 0.08	10.5	0.084
OEF	0.25 ± 0.02	0.36 ± 0.03	43.3	**0.007**
A (mm^{-1})	0.35 ± 0.03	0.37 ± 0.04	9.6	0.51
α	2.7 ± 0.1	3.9 ± 0.32	45.5	**0.025**

Table 1.3: Average parameters (mean ± standard error) of PHVD patients (N = 20) compared to controls (N = 13).

3.7 Error Analysis

The StO$_2$ measurements derived from the simulated data for the 2-layer model of the neonatal brain showed that StO$_2$ was increasingly underestimated as the CMT was reduced to less than 15 mm (Figure 3.7). This underestimation, based on a non-scattering CSF layer, did not change when the μ_a values for red or yellow CSF samples were used instead of the values for water.
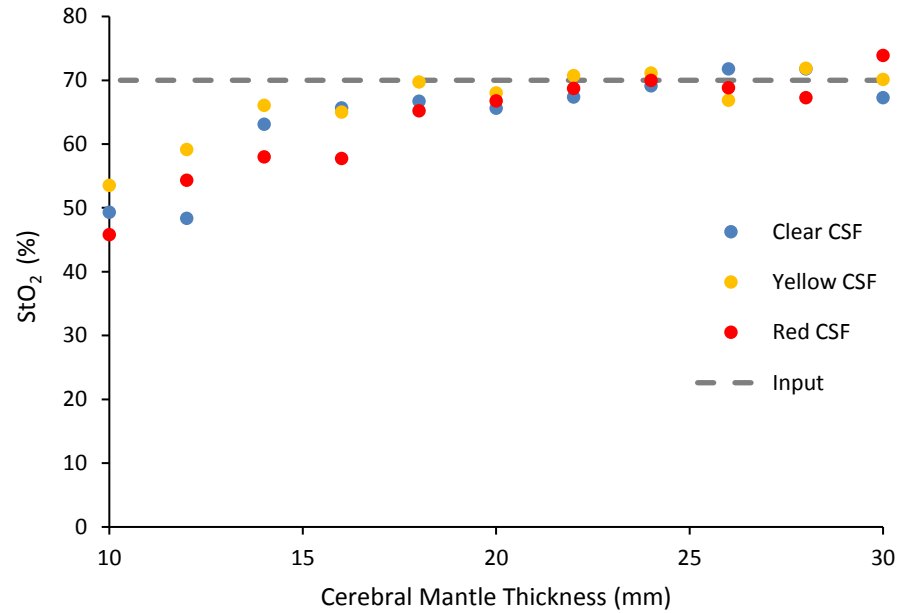
Figure 3.7: StO$_2$ versus cerebral mantle thickness generated from Monte Carle modelling for CSF with $\boldsymbol{\mu_a}$ values that reflect water (normal clear CSF), red and yellow CSF samples. Simulations show an underestimation of measured StO$_2$ as the CMT is decreased below 15 mm while the model oxygen saturation remains constant at 70%.

Chapter 4

4   Discussion

NIRS has been proposed as a method of monitoring biomarkers in the brain to guide the management of PHVD patients.[114] However, these patients have anatomical features that present challenges to NIRS. For this study the NIRS analysis method was modified to account for the thinning cerebral mantle caused by PHVD and the presence of BBPs in the ventricle space. This method was then applied to patients who were selected for VT based on clinical symptoms in order to investigate possible improvements in CBF and $CMRO_2$ due to ventricular decompression. Additionally, baseline NIRS measurements were compared to a control group without any major cerebral pathology. Finally, error analysis by Monte Carlo simulations was performed to predict errors when applying conventional NIRS analysis techniques to this unique patient population.

There is clear evidence from cranial US that the thickness of the brain is considerably reduced in PHVD patients. The mean CMT from the 9 patients enrolled in this study was 1.2 ± 0.1 cm with a range from 1 to 1.7 cm, whereas, the CMT in a normal preterm brain would typically be greater than 2 cm. To investigate how compressing the mantle could impact the accuracy of NIRS, Monte Carlo simulations were performed using a two-layer model to represent the cerebral mantle and the ventricular space. Reflectance data were generated for SDD of 3 and 4 cm, which are recommended to minimize signal contamination from superficial tissue, and used to estimate StO_2 by SRS. The simulations indicated that StO_2 was increasingly underestimated as the CMT approach 1 cm due to the loss of light into the ventricles, which is not accounted for when the brain is modelled as a semi-infinite medium (Figure 3.7). These simulations indicate that analysis methods used by common commercial NIRS systems should be interpreted with caution when applied to this patient population.

In this study, compression of the cortical mantle was accounted for by analyzing the measured spectra with a slab solution to the diffusion approximation, which is likely a more realistic description of light propagation through the head given the brain thickness

is not sufficient to be considered a semi-infinite volume. This approach takes advantage of the fact that the CMT can be estimated by readily available US images. Interestingly, the changes in the reflectance spectrum predicted by the slab model were similar to those observed experimentally (Figure 3.4).

A second consideration was the possibility of additional light absorption due to the presence of BBPs. To address this, absorption spectra from CSF samples were measured and incorporated into the fitting routine. Although, there are differences between the spectra for red and yellow CSF samples, their overall shapes were similar (Figure 3.2) and, therefore, the mean spectrum of all samples was used in the fitting procedure. Using a mean spectrum could result in errors due to time-dependent variations in the relative contributions of BBPs. However, it was found that characterizing the measured spectra was generally not improved by including $\mu_{a,BBP}(\lambda)$ as the best-fit estimate of the scaling factor k was close to zero. In only two cases did including k influence the fitting: pre-VT StO_2 dropped from 74 to 49% in one case and from 65 to 60% in the other when $\mu_{a,BBP}$ was excluded. In these cases, which were both classified as Grade IV IVH, bleeding into the brain may have affected light absorption. The negligible contribution of $\mu_{a,BBP}(\lambda)$ for all other patients can be explained by the low scattering properties of CSF, as indicated by the TR-NIRS results showing minimal light dispersion compared to water. In this case, the ventricles would act as a light 'sink' since the amount of back-scattered light in the ventricles would be insignificant. These findings are in agreement with the Monte Carlo results that showed similar StO_2 values across the range of CMTs regardless of whether $\mu_a(\lambda)$ of the CSF layer was set to values of water or those determined from CSF samples.

Regarding the clinical aim of this study, significant increases in CBF and [HbO_2] were found following VT, likely due to reduced ICP as suggested by the corresponding reduction in head circumference. This finding is in agreement with Doppler flow and NIRS oxygenation studies that reported increases in their respective measurements following similar interventions.[46,47,115] However, unlike previous studies that only provided indirect measures of CBF, such as the oxygenation difference signal (HbO_2 - Hb), the use of DCE NIRS enabled CBF to be measured directly. The benefits were not

only to confirm that CSF removal does improve CBF, but also to show that the perfusion change was fairly modest with a mean increase of 15%. To put this in context, the same DCE NIRS approach was used previously to show that CBF decreased by 20 to 30% in preterm infants administered the vasoconstrictor indomethacin as treatment for patent ductus arteriosus.[48,95] In that study, the reduction in CBF did not affect $CMRO_2$ due to a compensatory increase in OEF. In light of these previous findings, it is not surprising that no significant decompression-related change in $CMRO_2$ was found. Elevated OEF prior to VT would be expected to compensate for lower CBF. A trend towards a reduction in OEF after VT was observed, but it did not reach statistical significance. It is conceivable that extending the monitoring period may have detected subsequent changes in StO_2 and OEF. It is also possible that the slab solution to the diffusion approximation did not fully model light propagation through the head. This solution assumes planar geometry and factors such as the curvature of the head and variations in CMT could lead to errors. Monte Carlo simulations incorporating segmented head models could be used to address these issues but are beyond the scope of this study.[101]

The lack of an effect on cerebral energy metabolism is in line with Soul et al. who reported no change in cerebral cytochrome oxidase.[47] Unlike Norooz et al.[46], no significant change in StO_2 was observed with treatment, which could be related to differences in the type of treatment and timing of the measurements. The Norooz study used external ventricular drainage for decompression and StO_2 was measured 24 h after the procedure. Another discrepancy was that the mean pre-intervention StO_2 (43%) was considerably lower than the value found in the current study (59%). This could be explained by patient selection differences between the studies, or StO_2 may still be underestimated in the PHVD group due to uncertainty in US measurements of the CMT, although these measurement were made as close as possible to the NIRS probes to minimize errors.

Compared to the control group, PVHD patients had significantly lower StO_2 and higher OEF. These changes suggest reduced oxygen delivery, although it is not clear why treatment-related improvements were not detected considering the agreement between post-VT CBF and mean CBF from controls (16.9 versus 16.5 ml/100g/min, respectively).

A limitation is that StO_2 and OEF were only measured at single times, and it is conceivable that extending the monitoring could have detected further oxygenation changes. Alternately, StO_2 may still be underestimated in the PHVD group due to uncertainty in US measurements of the CMT, although these were made as close as possible to the NIRS probes to minimize errors. It is also possible that the slab solution to the diffusion approximation did not fully model light propagation through the head. This solution assumes planar geometry and factors such as the curvature of the head and variations in CMT could lead to errors. Monte Carlo simulations incorporating segmented head models could be used to address these issues but are beyond the scope of this study.[101] Interestingly, it was also found that the fitting parameter α was greater in PHVD patients compared to controls, suggesting that the compression of the cortical mantle can alter the scattering properties of the tissue.

Chapter 5

5 Summary

5.1 Limitations and Future Work

As mentioned in Chapter 4, a limitation with this study is that the DCE NIRS method only enabled CBF to be measured at single time points before and after the VT. Continuous CBF monitoring is possible using DCS and, in combination with DCE NIRS, the blood flow index can be converted into units of absolute CBF. The ability to monitor CBF and StO$_2$ over extended periods of time could be used to monitor disease progression in order to detect sudden hemodynamic and/or metabolic changes that indicate the need for clinical decompression. These functional measures could also be combined with ventricular volume measurements from 3D US to determine if there is a relationship between ventricular dilatation and cerebral perfusion and metabolism.[116] Likewise, continuous monitoring after a VT could help understand its long-term effects since it is conceivable that the benefits treatment with regards to cerebral function manifests a few hours afterwards.

Another potential limitation with this study was the difference between the location of the NIRS probes, which was on the scalp above the lateral-frontal region of the brain, and the location of the CMT measurements. These were of the fronto-parietal region from US images taken through the anterior fontanelle. Better imaging of the specific region interrogated by the NIRS probes could be performed by acquiring US images through the posterior fontanelle. However this location was not practical with these patients who often did not respond well to being moved, which would be required for imaging through the posterior fontanelle.

Finally the broadband NIRS data were collected at a single source-detector distance of 3 cm, which was chosen to limit contamination from extra-cerebral tissues. At this distance, the depth penetration of light is of the order of 1.7 cm (the square root of the separation). Potentially, reducing the SDD could limit ventricular contamination however this would increase extra-cerebral contamination. Monte Carlo simulations including an

extra-cerebral layer could be performed to determine the optimal SDD to minimize both sources of signal contamination. Alternatively, multi-distance measurements could be obtained to characterize signal contributions from each extra-cerebral, brain and ventricular regions.

5.2   Conclusions

In summary, this work presents a NIRS method for monitoring CBF and $CMRO_2$ in PHVD patients. The use of broadband NIRS, rather than a conventional system limited to measurements at a few wavelengths, enabled potential sources of error associated with this unique patient population to be investigated.

The spectral results, along with Monte Carlo simulations, demonstrated that the most significant source of error was the compression of the cortical mantle. The spectral analysis routine was modified to account for this effect by incorporating US measurements of the cerebral mantle as well as potential signal contamination from BBPs.

Using this patient-specific approach, it was found that VT was associated with a statistically significant increase in CBF and $[HbO_2]$, but had no significant effect on $CMRO_2$, likely reflecting a compensatory increase in the OEF. Compared to controls, PHVD was associated with significantly lower StO_2, lower $[HbO_2]$ and elevated OEF, which are indications of possible restricted oxygen delivery. These results suggest that NIRS could play a useful role is determining the impact of PHVD on patient health. Continuous monitoring achievable by incorporating diffuse correlation spectroscopy,[48,98,117] would be beneficial to investigate longer-term perfusion and metabolic changes leading up to and following clinical interventions such as VTs.

References

1.   Whitelaw A. A different view: There is value in grading intraventricular hemorrhage. *Acta Paediatr Int J Paediatr* 2007; 96: 1257–1258.

2.   Goldenberg RL, Jobe AH. Prospects for research in reproductive health and birth outcomes. *JAMA* 2001; 285: 633–639.

3.   Whitelaw a., Aquilina K. Management of posthaemorrhagic ventricular dilatation. *Arch Dis Child - Fetal Neonatal Ed* 2012; 97: F229–F233.

4.   Calisici E, Eras Z, Oncel MY, et al. Neurodevelopmental outcomes of premature infants with severe intraventricular hemorrhage. *J Matern Fetal Neonatal Med* 2014; 7058: 1–6.

5.   Olischar M, Klebermass K, Kuhle S, et al. Progressive posthemorrhagic hydrocephalus leads to changes of amplitude-integrated EEG activity in preterm infants. *Child's Nerv Syst* 2004; 20: 41–45.

6.   Radic JAE, Vincer M, McNeely PD. Outcomes of intraventricular hemorrhage and posthemorrhagic hydrocephalus in a population-based cohort of very preterm infants born to residents of Nova Scotia from 1993 to 2010. *J Neurosurg Pediatr* 2015; 15: 580–8.

7.   Synnes AR, Chien LY, Peliowski A, et al. Variations in intraventricular hemorrhage incidence rates among Canadian neonatal intensive care units. *J Pediatr* 2001; 138: 525–31.

8.   Sajjadian N, Fakhrai H, Jahadi R. Incidence of intraventricular hemorrhage and post hemorrhagic hydrocephalus in preterm infants. *Acta Med Iran* 2010; 48: 260–262.

9.   Ahn SY, Shim SY, Sung IK. Intraventricular hemorrhage and post hemorrhagic hydrocephalus among very-low-birth-weight infants in Korea. *J Korean Med Sci* 2015; 30: S52–S58.

10. Gould SJ, Howard S. Glial differentiation in the germinal layer of fetal and preterm infant brain: an immunocytochemical study. *Pediatr Pathol* 1988; 8: 25–36.

11. Ballabh P, Braun A, Nedergaard M. Anatomic analysis of blood vessels in germinal matrix, cerebral cortex, and white matter in developing infants. *Pediatr Res* 2004; 56: 117–124.

12. Braun A, Xu H, Hu F, et al. Paucity of pericytes in germinal matrix vasculature of premature infants. *J Neurosci* 2007; 27: 12012–24.

13. Ballabh P. NIH Public Access. *Pediatr Res* 2010; 67: 1–8.

14. Tauscher MK, Berg D, Brockmann M, et al. Association of histologic chorioamnionitis, increased levels of cord blood cytokines, and intracerebral hemorrhage in preterm neonates. *Biol Neonate* 2003; 83: 166–170.

15. Kassal R, Anwar M, Kashlan F, et al. Umbilical vein interleukin-6 levels in very low birth weight infants developing intraventricular hemorrhage. *Brain Dev* 2005; 27: 483–487.

16. Heep A, Behrendt D, Nitsch P, et al. Increased serum levels of interleukin 6 are associated with severe intraventricular haemorrhage in extremely premature infants. *Arch Dis Child Fetal Neonatal Ed* 2003; 88: F501-4.

17. Poralla C, Traut C, Hertfelder H-J, et al. The coagulation system of extremely preterm infants: influence of perinatal risk factors on coagulation. *J Perinatol* 2011; 32: 869–873.

18. Hagberg H, Mallard C, Ferriero DM, et al. The role of inflammation in perinatal brain injury. *Nat Rev Neurol* 2015; 11: 192–208.

19. Douglas-Escobar M, Weiss MD. 1. Douglas-Escobar M, Weiss MD. Biomarkers of brain injury in the premature infant. Front Neurol. 2012;3:185. Biomarkers of brain injury in the premature infant. *Front Neurol* 2012; 3: 185.

20. Andrikopoulou M, Almalki A, Farzin A, et al. Perinatal biomarkers in prematurity: Early identification of neurologic injury. *International Journal of Developmental Neuroscience* 2014; 36: 25–31.

21. Baier RJ. Genetics of perinatal brain injury in the preterm infant. *Front Biosci* 2006; 11: 1371–1387.

22. Ryckman KK, Dagle JM, Kelsey K, et al. Replication of genetic associations in the inflammation, complement, and coagulation pathways with intraventricular hemorrhage in LBW preterm neonates. *Pediatr Res* 2011; 70: 90–95.

23. Ment LR, Adén U, Lin A, et al. Gene-environment interactions in severe intraventricular hemorrhage of preterm neonates. *Pediatr Res* 2014; 75: 241–50.

24. Papile LA, Burstein J, Burstein R, et al. Incidence and evolution of subependymal and intraventricular hemorrhage: A study of infants with birth weights less than 1,500 gm. *J Pediatr* 1978; 92: 529–534.

25. Article R. Incidence of and risk factors for neonatal morbidity after active perinatal care: extremely preterm infants study in Sweden (EXPRESS). *Acta Paediatr* 2010; 99: 978–92.

26. Wilson-Costello D, Friedman H, Minich N, et al. Improved survival rates with increased neurodevelopmental disability for extremely low birth weight infants in the 1990s. *Pediatrics* 2005; 115: 997–1003.

27. Adams-Chapman I, Hansen NI, Stoll BJ, et al. Neurodevelopmental outcome of extremely low birth weight infants with posthemorrhagic hydrocephalus requiring shunt insertion. *Pediatrics* 2008; 121: e1167-77.

28.   Klebermass-Schrehof K, Czaba C, Olischar M, et al. Impact of low-grade intraventricular hemorrhage on long-term neurodevelopmental outcome in preterm infants. *Child's Nerv Syst* 2012; 28: 2085–2092.

29.   Futagi Y, Toribe Y, Ogawa K, et al. Neurodevelopmental outcome in children with intraventricular hemorrhage. *Pediatr Neurol* 2006; 34: 219–224.

30.   Bolisetty S, Dhawan A, Abdel-Latif M, et al. Intraventricular hemorrhage and neurodevelopmental outcomes in extreme preterm infants. *Pediatrics* 2014; 133: 55–62.

31.   Murphy BP, Inder TE, Rooks V, et al. Posthaemorrhagic ventricular dilatation in the premature infant: natural history and predictors of outcome. *Arch Dis Child Fetal Neonatal Ed* 2002; 87: 37–41.

32.   Limbrick DD, Mathur A, Johnston JM, et al. Neurosurgical treatment of progressive posthemorrhagic ventricular dilation in preterm infants: a 10-year single-institution study. *J Neurosurg Pediatr* 2010; 6: 224–30.

33.   Futagi Y, Suzuki Y, Toribe Y, et al. Neurodevelopmental outcome in children with posthemorrhagic hydrocephalus. *Pediatr Neurol* 2005; 33: 26–32.

34.   Hill A. Ventricular dilation following intraventricular hemorrhage in the premature infant. *Can J Neurol Sci* 1983; 10: 81–85.

35.   Guyer B, MacDorman MF, Martin JA, et al. Annual summary of vital statistics - 1997. *Pediatrics* 1998; 102: 1333–1349.

36.   Strahle J, Garton HJL, Maher CO, et al. Mechanisms of Hydrocephalus After Neonatal and Adult Intraventricular Hemorrhage. *Translational Stroke Research* 2012; 3: 25–38.

37.   Zhang J, Williams MA, Rigamonti D. Genetics of human hydrocephalus. *Journal of Neurology* 2006; 253: 1255–1266.

38. Del Bigio MR. Ependymal cells: Biology and pathology. *Acta Neuropathologica* 2010; 119: 55–73.

39. Krishnamurthy S, Li J, Schultz L, et al. Intraventricular infusion of hyperosmolar dextran induces hydrocephalus: a novel animal model of hydrocephalus. *Cerebrospinal Fluid Res* 2009; 6: 16.

40. Whitelaw A, Thoresen M, Pople I. Posthaemorrhagic ventricular dilatation. *Arch Dis Child Fetal Neonatal Ed* 2002; 86: F72-4.

41. Grasby DC, Esterman A, Marshall P. Ultrasound grading of cerebral ventricular dilatation in preterm neonates. *J Paediatr Child Health* 2003; 39: 186–90.

42. Jary S, De Carli A, Ramenghi LA, et al. Impaired brain growth and neurodevelopment in preterm infants with posthaemorrhagic ventricular dilatation. *Acta Paediatr Int J Paediatr* 2012; 101: 743–748.

43. Whitelaw a. Repeated lumbar or ventricular punctures in newborns with intraventricular hemorrhage. *Cochrane Database Syst Rev* 2001; CD000216.

44. Olischar M, Klebermass K, Hengl B, et al. Cerebrospinal fluid drainage in posthaemorrhagic ventricular dilatation leads to improvement in amplitude-integrated electroencephalographic activity. *Acta Paediatr Int J Paediatr* 2009; 98: 1002–1009.

45. Hill A, Volpe JJ. Decrease in pulsatile flow in the anterior cerebral arteries in infantile hydrocephalus. *Pediatrics* 1982; 69: 4–7.

46. Norooz F, Urlesberger B, Giordano V, et al. Decompressing posthaemorrhagic ventricular dilatation significantly improves regional cerebral oxygen saturation in preterm infants. *Acta Paediatr* 2015; 104: 663–669.

47. Soul JS, Eichenwald E, Walter G, et al. CSF Removal in Infantile Posthemorrhagic Hydrocephalus Results in Significant Improvement in Cerebral Hemodynamics. *Pediatr Res* 2004; 55: 872–876.

48. Diop M, Kishimoto J, Toronov V, et al. Development of a combined broadband near-infrared and diffusion correlation system for monitoring cerebral blood flow and oxidative metabolism in preterm infants. *Biomed Opt Express* 2015; 6: 3907–3918.

49. Kissack CM, Weindling AM. Peripheral blood flow and oxygen extraction in the sick, newborn very low birth weight infant shortly after birth. *Pediatr Res* 2009; 65: 462–467.

50. Yoxall CW, Weindling AM. Measurement of cerebral oxygen consumption in the human neonate using near infrared spectroscopy: cerebral oxygen consumption increases with advancing gestational age. *Pediatr Res* 1998; 44: 283–290.

51. Elwell CE, Owen-Reece H, Cope M, et al. Measurement of adult cerebral haemodynamics using near infrared spectroscopy. *Acta Neurochir Suppl* 1993; 59: 74–80.

52. Cui W, Wang N, Chance B. Study of photon migration depths with time-resolved spectroscopy. *Opt Lett* 1991; 16: 1632–4.

53. Chance B, Weber A. The steady state of cytochrome b during rest and after contraction in frog sartorius. *J Physiol* 1963; 169: 263–277.

54. FF Jobsis. Noninvasive, infrared monitoring of cerebral and myocardial oxygen sufficiency and circulatory parameters. *Science (80-)* 1977; 198: 1264–1267.

55. Brazy JE, Lewis D V., Mitnick MH, et al. Noninvasive Monitoring of Cerebral Oxygenation in Preterm Infants: Preliminary Observations. *Pediatrics* 1985; 75: 217–225.

56. Ferrari M, Giannini I, Sideri G, et al. Continuous non invasive monitoring of human brain by near infrared spectroscopy. *Oxyg Transp to Tissue VII* 1985; 191: 873–882.

57. Wyatt JS, Delpy DT, Cope M, et al. Quantification of Cerebral Oxygenation and Haemodynamics in Sick Newborn Infants by Near Infrared Spectrophotometry. *Lancet* 1986; 328: 1063–1066.

58. Cope M, Delpy DT, Reynolds EO, et al. Methods of quantitating cerebral near infrared spectroscopy data. *Adv Exp Med Biol* 1988; 222: 183–189.

59. Delpy DT, Cope M, van der Zee P, et al. Estimation of optical pathlength through tissue from direct time of flight measurement. *Phys Med Biol* 1988; 33: 1433–1442.

60. Siesler HW, Ozaki Y, Kawata S. *Near-Infrared Spectroscopy. Principles, Instruments, Applications*. 2002. Epub ahead of print 2002.

61. Cope M. *The Application of Near Infrared Spectroscopy to Non Invasive Monitoring of Cerebral Oxygenation in the Newborn Infant*. University College London, 1991.

62. Jacques SL. Optical properties of biological tissues: a review. *Phys Med Biol* 2013; 58: R37-61.

63. Wang RK. Modelling optical properties of soft tissue by fractal distribution of scatterers. *J Mod Opt* 2000; 47: 103–120.

64. Henyey, L. G. & Greenstein JL. Diffuse Radiation in the Galaxy. *Astrophys Journal, vol 93, p 70-83* 1941; 93: 70–83.

65. Boas DA, Culver J, Stott J, et al. Three dimensional Monte Carlo code for photon migration through complex heterogeneous media including the adult human head. *Opt Express* 2002; 10: 159–70.

66. Fang Q, Boas D a. Monte Carlo simulation of photon migration in 3D turbid media accelerated by graphics processing units. *Opt Express* 2009; 17: 20178–20190.

67. Fang Q, Boas DA. Monte Carlo simulation of photon migration in 3D turbid media accelerated by graphics processing units. *Opt Express* 2009; 17: 20178–20190.

68. Matcher SJ, Cooper CE. Absolute quantification of deoxyhaemoglobin concentration in tissue near infrared spectroscopy. *Phys Med Biol* 1994; 39: 1295–312.

69. Matcher SJ, Kirkpatrick PJ, Nahid K, et al. Absolute quantification methods in tissue near-infrared spectroscopy. *Proc. SPIE* 2389, Optical Tomography, Photon Migration, and Spectroscopy of Tissue and Model Media: Theory, Human Studies, and Instrumentation, 486 (May 30, 1995);

70. Farrell TJ, Patterson SM. A diffusion theory model of spatially resolved, steady-state diffuse reflectance for the noninvasive determination of tissue optical properties in vivo. *Medical Physics* 1992; 19: 879.

71. Liu H, Boas D a, Zhang Y, et al. Determination of optical properties and blood oxygenation in tissue using continuous NIR light. *Phys Med Biol* 1995; 40: 1983–1993.

72. Chance B, Leigh JS, Miyake H, et al. Comparison of time-resolved and -unresolved measurements of deoxyhemoglobin in brain. *Proc Natl Acad Sci U S A* 1988; 85: 4971–4975.

73. Chance B, Mans M, Sorge J, et al. A Phase Modulation System for Dual Wavelength Difference Spectroscopy of Hemoglobin Deoxygenation in Tissues. *SPIE Time-Resolved Laser Spectrosc Biochem II* 1990; 1204: 481–491.

74. Duncan A, Whitlock TL, Cope M, et al. Multiwavelength, wideband, intensity-modulated optical spectrometer for near-infrared spectroscopy and imaging. *Proc. SPIE* 1993; 1888: 248–257.

75. Fantini S, Franceschini M-A, Maier JS, et al. Frequency-domain multichannel optical detector for noninvasive tissue spectroscopy and oximetry. *Opt Eng* 1995; 34: 32.

76. Son I, Yazici B. Near infrared imaging and spectroscopy for brain activity monitoring. *Adv Sens with Secur Appl* 2006; 341–372.

77. Rolfe P. In vivo near-infrared spectroscopy. *Annu Rev Biomed Eng* 2000; 2: 715–754.

78. Matcher SJ, Cope M, Delpy DT. Use of the water absorption spectrum to quantify tissue chromophore concentration changes in near-infrared spectroscopy. *Phys Med Biol* 1994; 39: 177–96.

79. Qiao M, Latta P, Meng S, et al. Development of Acute Edema Following Cerebral Hypoxia-Ischemia in Neonatal Compared with Juvenile Rats Using Magnetic Resonance Imaging. *Pediatr Res* 2004; 55: 101–106.

80. Edvinsson L, MacKenzie ET, McCulloch J. *Cerebral Blood Flow and Metabolism*. Epub ahead of print 2002.

81. Hyttel-Sorensen S, Hessel TW, la Cour A, et al. A comparison between two NIRS oximeters (INVOS, OxyPrem) using measurement on the arm of adults and head of infants after caesarean section. *Biomed Opt Express* 2014; 5: 3671.

82. Boas D a., Franceschini M a. Haemoglobin oxygen saturation as a biomarker: the problem and a solution. *Philos Trans R Soc A Math Phys Eng Sci* 2011; 369: 4407–4424.

83. Kety SS, Schmidt CF. The Nitrous Oxide Method For The Quantitative Determination of Cerebral Blood Flow in Man: Theory, Procedure and Normal Values. *J Clin Invest* 1948; 27: 476–483.

84. Edwards AD, Wyatt JS, Richardson C, et al. Cotside measurement of cerebral blood flow in ill newborn infants by near infrared spectroscopy. *Lancet* 1988; 2: 770–771.

85.   Patel J, Marks K, Roberts I, et al. Measurement of cerebral blood flow in newborn infants using near infrared spectroscopy with indocyanine green. *Pediatr Res* 1998; 43: 34–39.

86.   Gora F, Shinde S, Elwell CE, et al. Noninvasive measurement of cerebral blood flow in adults using near-infrared spectroscopy and indocyanine green: a pilot study. *J Neurosurg Anesthesiol* 2002; 14: 218–222.

87.   Yoneya S, Saito T, Komatsu Y, et al. Binding properties of indocyanine green in human blood. *Invest Ophthalmol Vis Sci* 1998; 39: 1286–1290.

88.   Boas DA, Yodh AG. Spatially varying dynamical properties of turbid media probed with diffusing temporal light correlation. *J Opt Soc Am A* 1997; 14: 192–215.

89.   Durduran T, Zhou C, Buckley EM, et al. Optical measurement of cerebral hemodynamics and oxygen metabolism in neonates with congenital heart defects. *J Biomed Opt* 2014; 15: 37004.

90.   Cheung C, Culver JP, Takahashi K, et al. In vivo cerebrovascular measurement combining diffuse near-infrared absorption and correlation spectroscopies. *Phys Med Biol* 2001; 46: 2053.

91.   Verdecchia K, Diop M, Lee T-Y, et al. Quantifying the cerebral metabolic rate of oxygen by combining diffuse correlation spectroscopy and time-resolved near-infrared spectroscopy. *J Biomed Opt* 2013; 18: 27007.

92.   Greisen G. Cerebral blood flow in preterm infants during the first week of life. *Acta Paediatr Scand* 1986; 75: 43–51.

93.   Kissack CM, Garr R, Wardle SP, et al. Cerebral fractional oxygen extraction is inversely correlated with oxygen delivery in the sick, newborn, preterm infant. *J Cereb Blood Flow Metab* 2005; 25: 545–553.

94. Zaccanti G, Fabrizio Martelli; Samuele Del Bianco; Andrea Ismaelli; *Light Propagation through Biological Tissue and Other Diffusive Media: Theory, Solutions, and Software*. 2010.

95. Arora R, Ridha M, Lee DSC, et al. Preservation of the metabolic rate of oxygen in preterm infants during indomethacin therapy for closure of the ductus arteriosus. *Pediatr Res* 2013; 73: 713–8.

96. Verdecchia K, Diop M, Morrison LB, et al. Assessment of the best flow model to characterize diffuse correlation spectroscopy data acquired directly on the brain. *Biomed Opt Express* 2015; 6: 4288.

97. Milej D, Abdalmalak A, McLachlan P, et al. Subtraction-based approach for enhancing the depth sensitivity of time-resolved NIRS. *Biomed Opt Express* 2016; 7: 4514.

98. Diop M, Tichauer KM, Elliott JT, et al. Comparison of time-resolved and continuous-wave near-infrared techniques for measuring cerebral blood flow in piglets. *J Biomed Opt* 2011; 15: 57004.

99. Buiteveld H, Haakvort JHM, Donze M. The Optical Properties of Pure Water. In: *Proceedings of SPIE*. 1994, pp. 174–183.

100. Smith CR, Baker SK. Optical properties of the clearest natural waters (200?800 nm). *Appl Opt* 1981; 20: 177–184.

101. Dehaes M, Grant PE, Sliva DD, et al. Assessment of the frequency-domain multi-distance method to evaluate the brain optical properties: Monte Carlo simulations from neonate to adult. *Biomed Opt Express* 2011; 2: 552–67.

102. Diop M, Wright E, Toronov V, et al. Improved light collection and wavelet de-noising enable quantification of cerebral blood flow and oxygen metabolism by a low-cost, off-the-shelf spectrometer. *J Biomed Opt* 2014; 19: 57007.

103. Yeganeh HZ, Toronov V, Elliott JT, et al. Broadband continuous-wave technique to measure baseline values and changes in the tissue chromophore concentrations. *Biomed Opt Express* 2012; 3: 2761–70.

104. Diop M, Lawrence KS. Deconvolution method for recovering the photon time-of-flight distribution from time-resolved measurements. *Opt Lett* 2012; 37: 2358.

105. Zierler KL. Equations for Measuring Blood Flow By External Monitoring of Radioisotopes. *Circ Res* 1965; 16: 309–321.

106. Wang L, Jacques SL, Zheng L. MCML-Monte Carlo modeling of light transport in multi-layered tissues. *Comput Methods Programs Biomed* 1995; 47: 131–146.

107. Erik Alerstam SA-E. Monte Carlo Simulations of Light Transport in Tissue. 2008; 1–12.

108. Brigadoi S, Aljabar P, Kuklisova-Murgasova M, et al. A 4D neonatal head model for diffuse optical imaging of pre-term to term infants. *Neuroimage* 2014; 100: 385–394.

109. Okada E, Delpy DT. Near-infrared light propagation in an adult head model. II. Effect of superficial tissue thickness on the sensitivity of the near-infrared spectroscopy signal. *Appl Opt* 2003; 42: 2915–2922.

110. Metz AJ, Biallas M, Jenny C, et al. The effect of basic assumptions on the tissue oxygen saturation value of near infrared spectroscopy. In: *Advances in Experimental Medicine and Biology*. 2013, pp. 169–175.

111. Barrows LJ, Hunter FT, Banker BQ. The nature and clinical significance of pigments in the cerebrospinal fluid. *Brain* 1955; 78: 59–80.

112. Otterbein LE, Choi a M. Heme oxygenase: colors of defense against cellular stress. *Am J Physiol Lung Cell Mol Physiol* 2000; 279: 1029–1037.

113. Lee J, El-Abaddi N, Duke A, et al. Noninvasive in vivo monitoring of methemoglobin formation and reduction with broadband diffuse optical spectroscopy. *J Appl Physiol* 2006; 100: 615–622.

114. Elser HE, Holditch-Davis D, Brandon DH. Cerebral Oxygenation Monitoring: A Strategy to Detect IVH and PVL. *Newborn Infant Nurs Rev* 2011; 11: 153–159.

115. van Alfen-van der Velden AAEM, Hopman JCW, Klaessens JHGM, et al. Cerebral hemodynamics and oxygenation after serial CSF drainage in infants with PHVD. *Brain Dev* 2007; 29: 623–629.

116. Kishimoto J, Fenster A, Lee DSC, et al. In Vivo Validation of a 3-D Ultrasound System for Imaging the Lateral Ventricles of Neonates. *Ultrasound Med Biol* 2016; 42: 971–979.

117. Diop M, Verdecchia K, Lee T-Y, et al. Calibration of diffuse correlation spectroscopy with a time-resolved near-infrared technique to yield absolute cerebral blood flow measurements. *Biomed Opt Express* 2011; 2: 2068–2081.

Appendices

Appendix A: Ethics Approval Notice (REB)

Research Ethics

Western Research

Western University Health Science Research Ethics Board
HSREB Annual Continuing Ethics Approval Notice

Date: March 15, 2017
Principal Investigator: Dr. Sandrine de Ribaupierre
Department & Institution: Schulich School of Medicine and Dentistry\Clinical Neurological Sciences, Western University

Review Type: Full Board
HSREB File Number: 100315
Study Title: New technologies in the management of post-hemorrhagic hydrocephalus in preterm infants (REB #17827)

HSREB Renewal Due Date & HSREB Expiry Date:
Renewal Due -2018/03/31
Expiry Date -2018/04/05

The Western University Health Science Research Ethics Board (HSREB) has reviewed the Continuing Ethics Review (CER) Form and is re-issuing approval for the above noted study.

The Western University HSREB operates in compliance with the Tri-Council Policy Statement Ethical Conduct for Research Involving Humans (TCPS2), the International Conference on Harmonization of Technical Requirements for Registration of Pharmaceuticals for Human Use Guideline for Good Clinical Practice (ICH E6 R1), the Ontario Freedom of Information and Protection of Privacy Act (FIPPA, 1990), the Ontario Personal Health Information Protection Act (PHIPA, 2004), Part 4 of the Natural Health Product Regulations, Health Canada Medical Device Regulations and Part C, Division 5, of the Food and Drug Regulations of Health Canada.

Members of the HSREB who are named as Investigators in research studies do not participate in discussions related to, nor vote on such studies when they are presented to the REB.

The HSREB is registered with the U.S. Department of Health & Human Services under the IRB registration number IRB 00000940.

Curriculum Vitae

Name: Peter McLachlan

Post-secondary   Western University Canada
Education and   London, Ontario, Canada
Degrees: 2014-2017 MSc

                    The University of Western Ontario
                    London, Ontario, Canada
                    2011-2014 BMSc

                    The University of Waterloo
                    Waterloo, Ontario, Canada
                    2000-2006 BSc

Honours and   University of Western Ontario Gold Medal, Clinical Medical
Awards: Biophysics, 2014

                    Dean's Honour Roll – Western University, 2012, 2013

                    Waterloo Engineering Entrance Scholarship, 2000

Related Work   Teaching Assistant
Experience: The University of Waterloo
                    2003-2006

Publications:

P. McLachlan, J. Kishimoto, M. Diop, D. Milej, D.S.C. Lee, S. de Ribaupierre, K. St. Lawrence. Investigating the Effects of Cerebrospinal Fluid Removal on Cerebral Blood Flow and Oxidative Metabolism in Infants with Post-Hemorrhagic Ventricular Dilatation. Pediatric Research. 2017 (accepted)

Oral Presentations:

P. McLachlan, J. Kishimoto, M. Diop, D. Milej, D.S.C. Lee, S. de Ribaupierre, K. St. Lawrence. Development of a NIRS method to quantify cerebral perfusion and oxidative metabolism in preterm neonates with post hemorrhagic ventricle dilation. SPIE Photonics 2017

Poster Presentations:

P. McLachlan, J. Kishimoto, M. Diop, D. Milej, S. de Ribaupierre, D.S.C. Lee, K. St Lawrence. Perfusion and Metabolism Changes after Cerebrospinal Fluid Removal for Post-Hemorrhagic Ventricular Dilatation. London Health Research Day 2017, Canada

P. McLachlan, J. Kishimoto, M. Diop, S. de Ribaupierre, D.S.C. Lee, K. St Lawrence. The Pitfalls of Cerebral Oxygenation Monitoring in the Presence of Ventricular Dilatation. London Health Research Day 2016, Canada

P. McLachlan, J. Kishimoto, M. Diop, S. de Ribaupierre, D.S.C. Lee, K. St Lawrence The Pitfalls of Cerebral Oxygenation Monitoring in the Presence of Ventricular Dilatation Paediatric Academic Society Meeting 2015

J. Kishimoto, J. T. Elliot, **P. McLachlan**, M. Diop, S. de Ribaupierre, D.S.C. Lee, K. St. Lawrence. Monitoring Cerebral Blood Flow in Preterm Infants with Post-Hemorrhagic Hydrocephalus. The Optics Society – Biomedical Optics. April 26-30 2014. Miami, FL. US

P. McLachlan, J. Kishimoto, M. Diop, S. de Ribaupierre, D.S.C. Lee, K. St Lawrence. The Pitfalls of Cerebral Oxygenation Monitoring in the Presence of Ventricular Dilatation. London Health Research Day 2015, Canada

J. Kishimoto, M. Diop, **P. McLachlan**, S. de Ribaupierre, D.S.C. Lee, K. St Lawrence. Evidence of ventricular contamination of the optical signal in preterm neonates with post hemorrhagic ventricle dilation. SPIE – Photonics West 2015. February 7-12 2015. San Francisco, CA.

P. McLachlan, J. Kishimoto, M. Diop, S. de Ribaupierre, D.S.C. Lee, K. St Lawrence. The Contribution of Enlarged Ventricles to Cerebral Blood Flow Measurements of Preterm Neonates. London Health Research Day 2014, Canada

J. Kishimoto, M. Diop, **P. McLachlan**, S. de Ribaupierre, D.S.C. Lee, K. St Lawrence. Clinical Evidence of Ventricular Contamination in a NIRS Study of Post-Hemorrhagic Hydrocephalus in Preterm Infants. fNIRS 2014. October 10-12. Montreal, QU.